PROCEEDINGS A

royalsocietypublishing.org/journal/rspa

Research

Cite this article: Tang Y, Chu Y, Mei Y, Zhu Y, Liu K. 2026 Bar-and-hinge model for elasto-plastic origami analysis. *Proc. R. Soc. A* **482**: 20251119. https://doi.org/10.1098/rspa.2025.1119

Received: 29 December 2025
Accepted: 4 June 2026

Subject Areas:
structural engineering, mechanical engineering, mechanics

Keywords:
mechanics origami, elasto-plasticity, bar-and-hinge model, nonlinear analysis, large deformation, hysteresis

Author for correspondence:
Ke Liu
e-mail: liuke@pku.edu.cn

Bar-and-hinge model for elasto-plastic origami analysis

Yansong Tang[1], Yeqi Chu[2], Yue Mei[3], Yi Zhu[4] and Ke Liu[1]

[1]School of Advanced Manufacturing and Robotics, Peking University, Beijing 100871, People's Republic of China
[2]Department of Civil and Environmental Engineering, Princeton University, Princeton, NJ 08540, USA
[3]State Key Laboratory of Structural Analysis, Optimization and CAE Software for Industrial Equipment, Dalian University of Technology, Dalian 116024, People's Republic of China
[4]Department of Civil, Environmental, and Geospatial Engineering, Michigan Technological University, Houghton, MI 49931, USA

KL, 0000-0001-9081-6334

Origami-inspired structures are attracting considerable attention in engineering owing to their ability to facilitate intricate deformations and deployable configurations. However, accurately simulating their mechanical behaviour under realistic conditions involving permanent deformations and energy dissipation remains a significant challenge. In this study, we present an elasto-plastic formulation based on the nonlinear bar-and-hinge model for non-rigid origami simulation. We integrate rate-independent elasto-plastic constitutive models for both the hinges and the bars, enabling tunable representation of both elastic and plastic deformations in origami structures. The formulation employs a return mapping algorithm to ensure consistency with yield conditions checked at each incremental time step, enhancing numerical stability and accuracy. As a result, the proposed model provides realistic simulations by accurately reflecting the observed mechanical responses in real-world practice compared with purely elastic models. This formulation leads to MERLIN-PLAS, a new extension of the original MERLIN software, which minimizes the gap

THE ROYAL SOCIETY PUBLISHING

between idealized theoretical models and practical applications, providing a versatile and reliable simulation tool for functional origami-based systems.

1. Introduction

Tracing its origin to ancient art, origami has attracted increasing interest in recent decades, owing to its promising applications across scientific and engineering disciplines. The ability of origami structures to undergo large, programmable deformations has enabled their use in diverse fields such as metamaterials [1–3], aerospace systems [4–6], biomedical devices [7,8], Micro-Electro-Mechanical Systems (MEMS) [9,10] and robotics [11–14]. Recent advances further demonstrate the potential of origami and kirigami techniques in constructing complex three-dimensional electronic architectures, reconfigurable electromagnetic devices and morphable micro-air vehicles [15–18]. Although advanced fabrication techniques have been developed, mechanical testing of origami systems still depends on manual folding and carefully controlled loading protocols [19]. Within this framework, numerical modelling serves as an essential tool for predicting structural behaviour, guiding experimental design and elucidating underlying mechanical mechanisms.

Finite-element analysis (FEA) provides a direct method for simulating origami structures [20–25]. While FEA captures detailed material responses and delivers high-fidelity results, it often involves considerable computational expense and modelling effort, including extensive pre- and post-processing [26–29]. For example, shell elements, which are commonly used to model origami panels, tend to be computationally expensive and susceptible to numerical artefacts such as locking and instability [30–32]. Moreover, the use of connector elements to represent folding creases can introduce kinematic constraints that conflict with the rigid-body rotations of adjacent panels, resulting in over-constrained systems or numerical singularities during large rotations [33–35]. Consequently, simplified or reduced-order models have been developed to provide faster and more robust simulations, which are especially valuable during iterative design stages. Two representative approaches are the rigid origami simplification based on pure geometry [36–40], and the bar-and-hinge model based on solid mechanics [20,41–46]. The rigid origami simplification treats panels as rigid bodies connected by ideal frictionless hinges. This approach is computationally highly efficient and excels at analysing kinematic deployment paths, as demonstrated in generalized Miura-ori patterns [36,37]. However, its fundamental assumption precludes any material deformation, making it unsuitable for predicting the real-world responses of origami structures. By contrast, the bar-and-hinge model offers a mechanical framework by idealizing the structure as a pin-jointed truss with rotational springs. This model retains the fidelity needed to simulate both geometric and material nonlinearities. While existing implementations of this framework, such as MERLIN [47,48], have demonstrated computational efficiency and reliability in capturing hyperelastic responses [19,42,45,49–52], they fall short in representing irreversible phenomena such as plastic deformations. This limitation becomes particularly critical as research advances towards origami structures that exploit plasticity for energy dissipation [53–58]. Furthermore, important experimental observations in origami mechanics, such as hysteresis loops under cyclic loading [13,59–62], underscore the need for a numerical tool that can capture these effects. Therefore, extending the bar-and-hinge framework to include more general constitutive relations, notably elasto-plasticity, is crucial for reproducing the realistic mechanical behaviour of origami structures.

This article introduces an elasto-plastic bar-and-hinge formulation for realistic structural analysis of origami structures. Building upon the MERLIN framework [48], the proposed model incorporates rate-independent elasto-plastic constitutive relations for both bars and hinges, enabling tunable representation of both elastic and plastic deformations. The formulation employs a return mapping algorithm to ensure consistency with yield conditions at each incremental step, enhancing numerical stability and accuracy. As illustrated in figure 1, the

Table 1. Nomenclature.

Latin symbols	
A	cross-sectional area of bar element
A_i	cross-sectional area of bar i
C	tangential elastic modulus of bar
C_b	algorithmic tangent modulus for bar element
C_h	algorithmic tangent modulus for hinge element
E	Young's modulus of bar element
f	yield function
F_{ext}	external force vector
H	plastic modulus (general)
H_b	plastic modulus of bar element
$H_{h,f}$	plastic modulus of folding hinge
$H_{h,b}$	plastic modulus of bending hinge
k	rotational stiffness coefficient
k_0	elastic rotational modulus per unit length
k_f	stiffness of folding hinge
k_b	stiffness of bending hinge
K_T	tangent stiffness matrix
L	length of element
L_0	initial length
M	moment
S_X	second Piola–Kirchhoff stress
T	internal force vector
u	displacement
U	strain energy
W	strain energy density
Y_0	initial yield stress (bar) or initial yield moment (hinge)
Y_b	yield stress of bar element
$Y_{h,f}$	yield moment of folding hinge
$Y_{h,b}$	yield moment of bending hinge
Greek symbols	
α_b	hardening parameter for bar element
α_h	hardening parameter for hinge element
γ	plastic multiplier
$\Delta\gamma$	incremental plastic multiplier
ϵ	logarithmic strain
ϵ_e	elastic strain
ϵ_p	plastic strain

(*Continued.*)

https://royalsocietypublishing.org/journal/rspa Proc. R. Soc. A 482: 20251119

Table 1. (*Continued.*)

θ	rotation angle
θ_0	initial rotation angle
θ_e	elastic rotation angle
θ_p	plastic rotation angle
λ	stretch ratio
λ^e	elastic stretch
λ^p	plastic stretch
τ	Kirchhoff stress
algorithmic parameters	
$k_{\max}$	maximum number of iterations per increment
N_{tol}	tolerance for consecutive increment failures
$\beta_{\min}$	minimum step size reduction factor
$c_{\min}$	minimum damping factor for displacement updates
tol	convergence tolerance for displacement increment norm
h_i	step size at the i-th increment in Newton–Raphson algorithm
c_i	damping coefficient at the i-th iteration
β_i	step size reduction factor at the i-th increment
subscripts and superscripts	
e	elastic component (e.g. ϵ_e, θ_e)
p	plastic component
(e)	element-level quantity (e.g. $\mathbf{K}^{(e)}, L^{(e)}$)
etr	trial value
$n, n+1$	time step indices
i, j	element indices
f	folding hinge
b	bending hinge
x, y, z	Cartesian coordinate directions
matrices and vectors	
$\mathbf{B}_1$	linear strain–displacement matrix
$\mathbf{B}_2$	nonlinear strain–displacement matrix
$\mathbf{K}$	stiffness matrix
$\mathbf{K}_M$	material stiffness matrix
$\mathbf{K}_G$	geometric stiffness matrix
$\mathbf{u}$	displacement vector
$\mathbf{T}$	internal force vector
$\mathbf{F}$	external force vector
$\mathbf{R}$	residual force vector
$\nabla\theta$	rotation gradient vector
$\nabla^2\theta$	Hessian of rotation

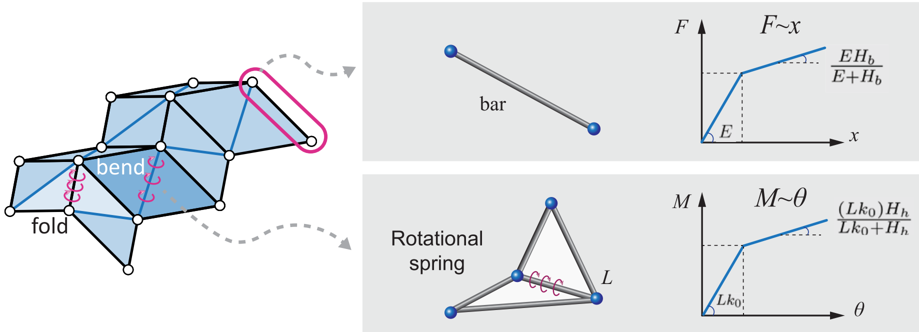

Figure 1. Bar-and-hinge model of an origami with elasto-plastic constitutive relation. For bar elements, the tangent stiffness decreases after yielding. For hinge elements, the rotational stiffness decreases when the rotational angle is large enough.

proposed framework is displacement based and accommodates both geometric and material nonlinearities, thereby establishing a comprehensive approach for both large-displacement and large-deformation analyses. The constitutive models are built upon rate-independent elasto-plasticity theories [63,64] with linear strain hardening. Through various numerical examples, we demonstrate the model's capability to capture essential elasto-plastic phenomena, including strain hardening and hysteresis loops.

The subsequent sections of this article are arranged as follows. Section 2 elaborates on the elasto-plastic constitutive models for different elements and the associated return mapping algorithm. Section 3 describes the numerical implementation, with specific attention to the displacement-loading mode. The force-loading mode is not repeated here, as it is thoroughly addressed in prior literature [47]. Section 4 is devoted to numerical examples of various origami structures. Finally, the concluding remarks are provided in §5 (table 1).

2. Elasto-plastic bar-and-hinge model

This section provides a comprehensive description of a rate-independent finite strain elasto-plastic model with isotropic hardening, developed for both bar and hinge elements. The formulation begins by decomposing the total strain into elastic and plastic components. The flow rule and yield condition are then derived from the principle of maximum plastic dissipation. To ensure numerical robustness and accuracy, the return mapping algorithm is introduced, which enforces consistency with the yield condition at each time step. Specific constitutive relations and their numerical implementation are subsequently detailed for both bars and hinges. The integration of these theoretical and numerical components yields a complete framework capable of simulating the elasto-plastic structural response under complex loading conditions.

(a) Constitutive relationship for bar elements

We adopt a finite-deformation kinematic description for bars. For a bar, the stretch $\lambda = L/L_0$ is decomposed multiplicatively into elastic and plastic parts as

$$\lambda = \lambda_e \lambda_p. \tag{2.1}$$

Taking the logarithmic strain $\epsilon = \ln \lambda$ converts this multiplicative decomposition into an additive one:

$$\epsilon = \epsilon_e + \epsilon_p, \quad \text{with } \epsilon = \ln \lambda,\ \epsilon_e = \ln \lambda_e,\ \epsilon_p = \ln \lambda_p. \tag{2.2}$$

This allows us to employ a standard small-strain plasticity framework in the material law while retaining exact finite-deformation kinematics. The algorithm is depicted in figure 2 [65,66].

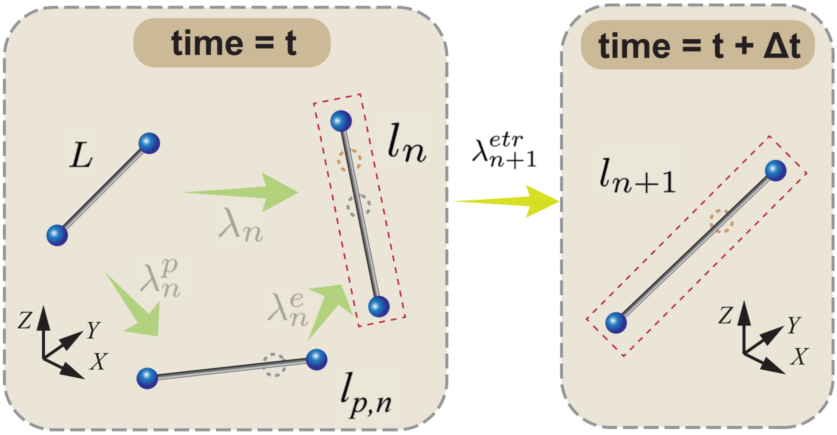

Figure 2. Mapping algorithm for bar elements: decomposition of stretch into elastic and plastic components at moment t, followed by the addition of trial elastic stretching to the existing plastic deformation at moment $t + \Delta t$.

We now adopt the small-strain additive decomposition within the logarithmic strain space. The plastic strain is obtained by integrating the plastic strain rate:

$$\epsilon_p = \int_0^t \dot{\epsilon}_p \, \mathrm{d}t. \tag{2.3}$$

The hardening parameter is defined as the accumulated absolute plastic strain:

$$\alpha_b = \int_0^t \dot{\alpha}_b \, dt, \qquad \dot{\alpha}_b = |\dot{\epsilon}_p| \, . \tag{2.4}$$

According to the maximum plastic dissipation principle, the one-dimensional flow rule is given by:

$$\dot{\epsilon}_p = \dot{\gamma}_b \frac{\partial f_b}{\partial \tau}, \tag{2.5}$$

where τ is the Kirchhoff stress, $\dot{\gamma}_b$ the plastic multiplier and f_b the yield function. For small strains, the yield condition takes the form:

$$f_b(\tau) = |\tau| - (Y_{b,0} + H_b \alpha_b) \leq 0, \tag{2.6}$$

where $Y_{b,0}$ is the initial yield stress and H is the plastic modulus. We enforce the yield condition at each increment using the return mapping algorithm [63].

In the absence of plastic flow, a trial state is assumed in which the deformation increment is purely elastic. The stretch at step $n + 1$ is then expressed multiplicatively as follows:

$$\lambda_{n+1} = \lambda_{n+1}^{\mathrm{etr}} \lambda_n^p, \tag{2.7}$$

where λ_n^p is the plastic stretch from the previous step. Correspondingly, the logarithmic strain decomposition becomes:

$$\epsilon_{n+1} = \ln(\lambda_{n+1}) = \ln(\lambda_{n+1}^{\mathrm{etr}}) + \ln(\lambda_n^p) = \epsilon_{n+1}^{\mathrm{etr}} + \epsilon_n^p. \tag{2.8}$$

If plastic deformation occurs, the incremental plastic strain is obtained via the backward Euler rule:

$$\Delta\epsilon_p \approx \dot{\epsilon}_{n+1}^p \Delta t = \Delta\gamma_b \, \mathrm{sign}(\tau_{n+1}), \tag{2.9}$$

with $\Delta\gamma_b = \dot{\gamma}_{b,n+1} \Delta t$. The hardening parameter is updated accordingly:

$$\alpha_{b,n+1} = \alpha_{b,n} + \Delta\gamma_b. \tag{2.10}$$

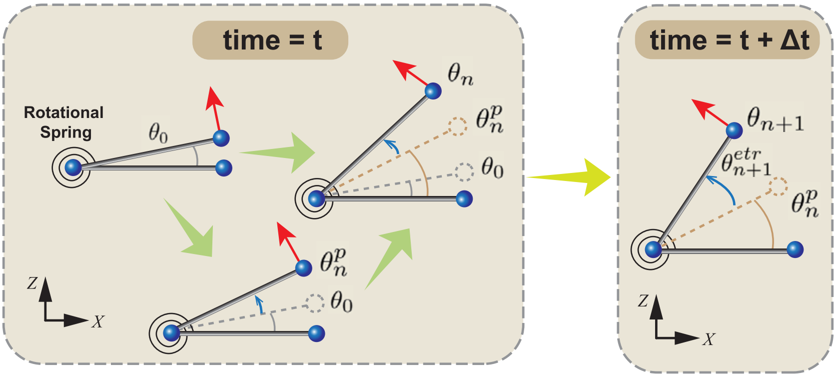

Figure 3. Return mapping algorithm for hinge elements: decomposition of rotation into elastic and plastic components at moment t, followed by the addition of trial elastic rotation to the existing plastic deformation at moment $t+\Delta t$.

(b) Constitutive relationship for hinge elements

The elasto-plastic response of a hinge mirrors that of a bar, except that its degrees of freedom are rotational angles and its conjugate variable is torque. Initially, the hinge experiences an applied torque, causing it to rotate elastically. When the torque reaches the yield torque, plastic rotation begins and a hardening component is activated in addition to the elastic response. The total rotation is then decomposed into elastic and plastic parts. Upon unloading, the elastic rotation and torque return to zero, while the plastic rotation remains, and the yield torque is permanently increased by the accumulated plastic moment. The update algorithm is shown in figure 3.

The elastic moment is governed by the elastic angle as follows:

$$M = k(\theta_e - \theta_0) = k[(\theta - \theta_0) - (\theta_p - \theta_0)], \tag{2.11}$$

where k is the rotational elastic stiffness and $\theta, \theta_e, \theta_p$ and θ_0 are the rotation angle, elastic angle, plastic angle and initial angle, respectively. The plastic angle θ_p in equation (2.11) is a path-dependent quantity, which needs to be obtained through time integration.

$$\theta_p = \int_0^t \dot{\theta}_p dt. \tag{2.12}$$

According to the flow rule,

$$\dot{\theta}_p = \dot{\gamma}_h \frac{\partial f_h}{\partial M}, \tag{2.13}$$

where $\dot{\gamma}_h$ is the plastic multiplier and f_h is the yield condition. The rotational yield condition is given as follows:

$$f_h(M) = |M| - (Y_{h,0} + H_h\alpha_h) \leq 0, \tag{2.14}$$

where L is the length of hinge, $Y_{h,0}$ is the initial yield moment, H_h is the plastic stiffness and α_h is the hardening parameter. Since $\partial f/\partial M = \mathrm{sign}(M)$, we have

$$\dot{\gamma}_h = |\dot{\theta}_p|. \tag{2.15}$$

α_h is defined as the accumulated absolute plastic angle occurring over time:

$$\alpha_h = \int_0^t |\dot{\theta}_p| dt. \tag{2.16}$$

In each incremental step, the integral in equation (2.16) is approximated similarly to those of §2a. By combining the backward Euler rule with the one-dimensional flow rule, the increment of the hardening parameters is:

$$\alpha_{h,n+1} = \alpha_{h,n} + \Delta\gamma_h. \tag{2.17}$$

(c) Numerical implementation for bars

Based on the multiplicative decomposition of the stretch (2.1) and the additive decomposition of logarithmic strain (2.2), the numerical return mapping algorithm proceeds as follows.

To start the next pseudo-time iteration $n+1$, we define the trial stretch and the logarithmic strain:

$$\lambda^{\mathrm{etr}}_{n+1} = \frac{\lambda_{n+1}}{\lambda^{p}_{n}} \tag{2.18}$$

and

$$\epsilon^{\mathrm{etr}}_{n+1} = \ln(\lambda^{\mathrm{etr}}_{n+1}), \tag{2.19}$$

where λ^{p}_{n} is the plastic stretch from the last pseudo-time iteration. In iteration $n+1$, the trial Kirchhoff stress and flow condition are given by

$$\tau^{\mathrm{etr}}_{n+1} = E\epsilon^{\mathrm{etr}}_{n+1}, \tag{2.20}$$

$$\tau_{n+1} = \tau^{etr}_{n+1} - E\Delta\gamma_b \operatorname{sgn}(\tau^{etr}_{n+1}), \tag{2.21}$$

and

$$f^{etr}_{b,n+1} = |\tau^{etr}_{n+1}| - (Y_{b,0} + H_b\alpha^{etr}_{b,n}), \tag{2.22}$$

where $\alpha^{\mathrm{etr}}_{b,n}$ is determined from the last pseudo-time iteration.

In the case of permanent deformation at a single time step, $-E\Delta\epsilon_p$ can be seen as a correction of the trial stress $\tau^{\mathrm{etr}}_{n+1}$. Loading/unloading conditions are determined by the trial yield function to check whether plastic correction is required. In the event of additional permanent deformation, $\Delta\epsilon_p$ will be determined by the incremental form of the flow rule, which requires the calculation of the incremental plastic multiplier $\Delta\gamma_b$.

In the plastic regime, we need to determine the incremental plasticity multiplier $\Delta\gamma_b$ and the $\operatorname{sign}(\tau_{n+1})$ such that the yield criterion $f(\tau_{n+1}, \alpha_{n+1}) = 0$ is satisfied. Rewriting equation (2.21) and gathering terms gives

$$(|\tau_{n+1}| + E\Delta\gamma_b)\operatorname{sign}(\tau_{n+1}) = |\tau^{\mathrm{etr}}_{n+1}|\operatorname{sign}(\tau^{\mathrm{etr}}_{n+1}). \tag{2.23}$$

Enforcing $f(\tau_{n+1}, \alpha_{n+1}) = 0$ implies $\Delta\gamma > 0$. The formula can be simplified into

$$\operatorname{sign}(\tau_{n+1}) = \operatorname{sign}(\tau^{\mathrm{etr}}_{n+1}) \quad \text{and} \quad |\tau_{n+1}| = |\tau^{\mathrm{etr}}_{n+1}| - E\Delta\gamma_b. \tag{2.24}$$

Combining equations (2.6), (2.10) and (2.24), the yield function at $n+1$ can be simplified as follows:

$$\begin{aligned} f_b(\tau_{n+1}, \alpha_{b,n+1}) &= |\tau_{n+1}| - (Y_{b,0} + H_b\alpha_{b,n+1}) \\ &= |\tau^{\mathrm{etr}}_{n+1}| - E\Delta\gamma_b - (Y_{b,0} + H_b\alpha_{b,n}) - H_b\Delta\gamma_b \\ &= |\tau^{\mathrm{etr}}_{n+1}| - (Y_{b,0} + H_b\alpha_{b,n}) - (E + H_b)\Delta\gamma_b \\ &= f^{etr}_{b,n+1} - (E + H_b)\Delta\gamma_b. \end{aligned} \tag{2.25}$$

Since $f(\tau_{n+1}, \alpha_{n+1}) = 0$, the incremental plastic multiplier can be found as follows:

$$\Delta\gamma_b = \frac{f^{\mathrm{etr}}_{b,n+1}}{E + H_b}. \tag{2.26}$$

Note that the incremental plastic multiplier is only a function of the trial elastic stress and the hardening parameter at time step n. Therefore, the update operation of the elastic–plastic parameters can be completed.

With $f^{\mathrm{etr}}_{b,n+1}$, we can determine whether the bar is elastic or plastic and further derive stress and tangent modulus:

— $f^{\mathrm{etr}}_{b,n+1} < 0$, elastic

(i) Second Piola–Kirchhoff stress: $S_{x,n+1} = \tau^{\mathrm{etr}}_{n+1}/\lambda^2$

(ii) Tangent modulus: $H_{n+1} = (E - 2\tau^{\mathrm{etr}}_{n+1})/\lambda^4$

— $f^{\text{etr}}_{b,n+1} > 0$, plastic

(i) Increment of the consistency parameter: $\Delta\gamma_{b,n+1} = f^{\text{etr}}_{b,n+1}/(E + H_b)$
(ii) Elastic strain: $\epsilon^e_{n+1} = \epsilon^{\text{etr}}_{n+1} - \Delta\gamma_{b,n+1}(\tau^{\text{etr}}_{n+1}/|\tau^{\text{etr}}_{n+1}|)$
(iii) Hardening parameter: $\alpha_{b,n+1} = \alpha_{b,n} + \Delta\gamma_{b,n+1}$
(iv) Kirchhoff stress: $\tau_{n+1} = E\epsilon^e_{n+1}$
(v) Algorithmic tangent modulus $C_b = EH_b/(E + H_b)$
(vi) Update of the plastic variables: $\lambda^p_{n+1} = \lambda_{n+1}/\exp(\epsilon^e_{n+1})$
(vii) Second Piola–Kirchhoff stress: $S_{x,n+1} = \tau_{n+1}/\lambda^2$
(viii) Tangent modulus: $H_{n+1} = (C_b - 2\tau_{n+1})/\lambda^4$

(d) Numerical implementation for hinges

Hinges are considered elasto-plastic rotational springs. The rotation is decomposed as

$$\theta - \theta_0 = (\theta_e - \theta_0) + (\theta_p - \theta_0). \tag{2.27}$$

To start the next pseudo-time iteration $n + 1$, we define the trial angle:

$$\theta^{\text{etr}}_{n+1} = \theta_{n+1} - \theta^p_n + \theta_0, \tag{2.28}$$

here θ^p_n is the plastic angle from the last pseudo-time iteration.

The trial moment and flow conditions for hinge rotation are

$$M^{\text{etr}}_{n+1} = Lk_0(\theta^{\text{etr}}_{n+1} - \theta_0) \tag{2.29}$$

and

$$f^{\text{etr}}_{h,n+1} = |M^{\text{etr}}_{n+1}| - (Y_{h,0} + H_h\alpha^{\text{etr}}_{h,n}) \le 0, \tag{2.30}$$

where L is the hinge length, k_0 is the elastic rotational modulus per unit length and Lk_0 is the total elastic rotational stiffness. $\alpha^{\text{etr}}_{h,n}$ is determined from the last pseudo-time iteration.

With $f^{\text{etr}}_{h,n+1}$, we determine whether the hinge is elastic or plastic and derive the stress and tangent modulus:

— $f^{\text{etr}}_{h,n+1} < 0$, elastic

(i) Moment: $M_{n+1} = M^{\text{etr}}_{n+1}$
(ii) Tangent modulus: $C_h = Lk_0$

— $f^{\text{etr}}_{h,n+1} > 0$, plastic

(i) Increment of the consistency parameter: $\Delta\gamma_{h,n+1} = f^{\text{etr}}_{h,n+1}/(Lk_0 + H_h)$
(ii) Elastic angle: $\theta^e_{n+1} = \theta^{\text{etr}}_{n+1} - \Delta\gamma_{h,n+1}(M^{\text{etr}}_{n+1}/|M^{\text{etr}}_{n+1}|)$
(iii) Hardening parameter: $\alpha_{h,n+1} = \alpha_{h,n} + \Delta\gamma_{h,n+1}$
(iv) Moment: $M_{n+1} = Lk_0(\theta^e_{n+1} - \theta_0)$
(v) Algorithmic tangent modulus: $C_h = (Lk_0)H_h/(Lk_0 + H_h)$
(vi) Update of plastic angle: $\theta^p_{n+1} = \theta_{n+1} - \theta^e_{n+1} + \theta_0$

(e) Linearized formulation of stiffness matrices and equilibrium equations

This section presents a derivation of the stiffness matrices and equilibrium equations for the elasto-plastic bar-and-hinge elements through linearization. The formulation is based on direct differentiation of the internal force expressions, avoiding energy-based methods to maintain consistency with the displacement-based framework.

(i) Bar element formulation

The internal force vector for a bar element is expressed as follows:

$$\mathbf{T}^{(e)}_{\mathrm{bar}} = \frac{\tau}{\lambda^2} A^{(e)} L^{(e)}_0 (\mathbf{B}_1 + \mathbf{B}_2 \mathbf{u}^{(e)}), \tag{2.31}$$

where τ denotes the Kirchhoff stress, λ represents the stretch ratio and $A^{(e)}$ is the cross-sectional area. The reference length $L^{(e)}_0$ corresponds to the undeformed configuration. The linear strain–displacement matrix $\mathbf{B}_1$ is defined as follows:

$$\mathbf{B}_1 = \frac{1}{L_0} \begin{bmatrix} -\mathbf{n}^T & \mathbf{n}^T \end{bmatrix}, \tag{2.32}$$

while the nonlinear strain–displacement matrix $\mathbf{B}_2$ takes the form:

$$\mathbf{B}_2 = \frac{1}{(L^{(e)}_0)^2} \begin{bmatrix} \mathbf{I} & -\mathbf{I} \\ -\mathbf{I} & \mathbf{I} \end{bmatrix}. \tag{2.33}$$

The element displacement vector $\mathbf{u}^{(e)}$ describes the current nodal positions.

The equilibrium condition requires:

$$\mathbf{T}^{(e)}_{\mathrm{bar}} - \mathbf{F}^{(e)}_{\mathrm{ext}} = \mathbf{0}, \tag{2.34}$$

with $\mathbf{F}^{(e)}_{\mathrm{ext}}$ representing the externally applied force vector. Linearization of this equilibrium state yields:

$$\mathrm{d}\mathbf{T}^{(e)}_{\mathrm{bar}} = \mathrm{d}\mathbf{F}^{(e)}_{\mathrm{ext}}. \tag{2.35}$$

The differential of the internal force vector is obtained through consistent differentiation:

$$\mathrm{d}\mathbf{T}^{(e)}_{\mathrm{bar}} = \frac{\partial \mathbf{T}^{(e)}_{\mathrm{bar}}}{\partial \mathbf{u}^{(e)}} \,\mathrm{d}\mathbf{u}^{(e)} + \frac{\partial \mathbf{T}^{(e)}_{\mathrm{bar}}}{\partial \tau} \,\mathrm{d}\tau. \tag{2.36}$$

The partial derivatives evaluate to:

$$\frac{\partial \mathbf{T}^{(e)}_{\mathrm{bar}}}{\partial \mathbf{u}^{(e)}} = \frac{\tau}{\lambda^2} A^{(e)} L^{(e)}_0 \mathbf{B}_2 \tag{2.37}$$

and

$$\frac{\partial \mathbf{T}^{(e)}_{\mathrm{bar}}}{\partial \tau} \,\mathrm{d}\tau = A^{(e)} L^{(e)}_0 (\mathbf{B}_1 + \mathbf{B}_2 \mathbf{u}^{(e)}) \frac{1}{\lambda^2} \,\mathrm{d}\tau. \tag{2.38}$$

The stress differential $\mathrm{d}\tau$ relates to the elastic strain increment through the algorithmic tangent modulus C_b:

$$\mathrm{d}\tau = C_b \,\mathrm{d}\epsilon_e = C_b \mathbf{B}_1^T \,\mathrm{d}\mathbf{u}^{(e)}, \tag{2.39}$$

where $C_b = E$ in elastic deformation and $C_b = EH_b/(E + H_b)$ in plastic deformation. Combining these expressions yields the complete differential expression:

$$\mathrm{d}\mathbf{T}^{(e)}_{\mathrm{bar}} = \frac{\tau}{\lambda^2} A^{(e)} L^{(e)}_0 \mathbf{B}_2 \,\mathrm{d}\mathbf{u}^{(e)} + A^{(e)} L^{(e)}_0 \frac{1}{\lambda^2} (\mathbf{B}_1 + \mathbf{B}_2 \mathbf{u}^{(e)}) C_b \mathbf{B}_1^T \,\mathrm{d}\mathbf{u}^{(e)}, \tag{2.40}$$

which separates into geometric and material stiffness contributions.

The tangent stiffness matrix therefore comprises:

$$\mathbf{K}_{\text{bar}}^{(e)} = \mathbf{K}_M^{(e)} + \mathbf{K}_G^{(e)}, \tag{2.41}$$

with the material stiffness matrix

$$\mathbf{K}_M^{(e)} = A^{(e)} L_0^{(e)} C_b \mathbf{B}_1 \mathbf{B}_1^T, \tag{2.42}$$

and the geometric stiffness matrix

$$\mathbf{K}_G^{(e)} = S_X A^{(e)} L_0^{(e)} \mathbf{B}_2, \tag{2.43}$$

where $S_X = \tau/\lambda^2$ is the second Piola–Kirchhoff stress. The combined expression is:

$$\mathbf{K}_{\text{bar}}^{(e)} = A^{(e)} L_0^{(e)} (C_b \mathbf{B}_1 \mathbf{B}_1^T + S_X \mathbf{B}_2). \tag{2.44}$$

(ii) Hinge element formulation

The internal force vector for a hinge element is defined as follows:

$$\mathbf{T}_{\text{spr}} = M \nabla\theta, \tag{2.45}$$

where M denotes the moment, and $\nabla\theta$ represents the gradient of the rotation angle θ with respect to the nodal displacement vector $\mathbf{u}$, i.e., $\nabla\theta = \partial\theta/\partial\mathbf{u}$. This formulation establishes the work–conjugate relationship between moment and rotation through the virtual work principle $\delta W_{\text{int}} = M \cdot \delta\theta$.

The equilibrium condition requires the vanishing residual:

$$\mathbf{T}_{\text{spr}} - \mathbf{M}_{\text{ext}} = \mathbf{0}, \tag{2.46}$$

where $\mathbf{M}_{\text{ext}}$ signifies the externally applied moment vector. Linearization of this equilibrium equation about the current configuration yields:

$$\mathrm{d}\mathbf{T}_{\text{spr}} = \mathrm{d}\mathbf{M}_{\text{ext}}. \tag{2.47}$$

The differential of the internal force vector is obtained through direct differentiation:

$$\mathrm{d}\mathbf{T}_{\text{spr}} = \frac{\partial}{\partial\mathbf{u}}(M\nabla\theta)\,\mathrm{d}\mathbf{u}. \tag{2.48}$$

Application of the product rule gives:

$$\mathrm{d}\mathbf{T}_{\text{spr}} = \left(\frac{\partial M}{\partial\mathbf{u}} \cdot \nabla\theta + M\frac{\partial(\nabla\theta)}{\partial\mathbf{u}}\right)\mathrm{d}\mathbf{u} \tag{2.49}$$

$$= \left(\frac{\partial M}{\partial\theta}\frac{\partial\theta}{\partial\mathbf{u}} \otimes \nabla\theta + M\nabla^2\theta\right)\mathrm{d}\mathbf{u}. \tag{2.50}$$

Substituting the rotational tangent modulus $C_h = \partial M/\partial\theta$ recalling the definition of $\nabla\theta$ produces

$$\mathrm{d}\mathbf{T}_{\text{spr}} = C_h(\nabla\theta \otimes \nabla\theta)\,\mathrm{d}\mathbf{u} + M\nabla^2\theta\,\mathrm{d}\mathbf{u}. \tag{2.51}$$

The rotational tangent modulus C_h takes the value Lk_0 in elastic deformation and $C_h = \frac{(Lk_0)H_h}{Lk_0+H_h}$ in plastic deformation, consistent with the constitutive models established in §2d.

The complete tangent stiffness matrix for the hinge element is therefore:

$$\mathbf{K}_{\text{spr}}^{(r)} = C_h \nabla\theta \otimes \nabla\theta + M\nabla^2\theta, \tag{2.52}$$

where the first term represents the material stiffness and the second term corresponds to the geometric stiffness. The Hessian $\nabla^2\theta$ captures the second-order geometric effects induced by finite rotations.

(iii) Stiffness matrix assembly and solution scheme

The global equilibrium equations are assembled through standard finite-element procedures:

$$\mathbf{R} = \mathbf{F}_{\text{int}} - \mathbf{F}_{\text{ext}} = \mathbf{0}, \tag{2.53}$$

where $\mathbf{F}_{\text{int}}$ represents the assembled internal force vector and $\mathbf{F}_{\text{ext}}$ denotes the global external force vector. The tangent stiffness matrix is assembled as:

$$\mathbf{K}_T = \sum_{e=1}^{N_e} \mathbf{K}_{\text{bar}}^{(e)} \oplus \sum_{r=1}^{N_r} \mathbf{K}_{\text{spr}}^{(r)}, \tag{2.54}$$

where $\oplus$ indicates the finite-element assembly operation that accounts for connectivity and degrees of freedom mapping between elements.

The nonlinear system is solved using the adaptive damped Newton–Raphson method presented in Algorithm 1. At iteration k, the solution increment is computed by solving:

$$\mathbf{K}_T^{(k)} \Delta\mathbf{u}^{(k)} = -\mathbf{R}^{(k)}, \tag{2.55}$$

followed by the displacement update:

$$\mathbf{u}^{(k+1)} = \mathbf{u}^{(k)} + c^{(k)} \Delta\mathbf{u}^{(k)}, \tag{2.56}$$

where $c^{(k)} \in (0, 1]$ is an adaptive damping coefficient that ensures numerical stability during plastic deformation processes. The residual vector $\mathbf{R}^{(k)}$ is recomputed at each iteration until the convergence criteria are satisfied.

3. Nonlinear equation solver

The present formulation incorporates two distinct solvers based on complementary numerical algorithms. The *Force* mode utilizes an augmented generalized displacement control method [47,67,68] to enhance numerical stability in path-following analysis. By contrast, the *Displacement* mode employs an adaptively damped Newton–Raphson scheme, with the complete mathematical formulation detailed in Algorithm 1. This dual-solver architecture ensures robust convergence for a wide range of nonlinear mechanical systems.

4. Origami simulations

This section demonstrates the application of the elasto-plastic bar-and-hinge model through a series of numerical examples on diverse origami structures. The analysis begins with a simple foldable mechanism, where the formulation is calibrated and validated against high-fidelity finite-element simulations. The study then progresses to an Eggbox pattern to examine residual-stress-driven non-Euclidean folding, followed by the Sareh twist as a fundamental twisting unit. Subsequently, the energy dissipation during mode switching in the Morph origami and the local bistability of the Miura-ori are investigated. Finally, the cyclic loading response and hysteresis behaviour of the Kresling origami structure are presented.

Before presenting the individual examples, we briefly describe the standardized procedure used to calibrate the plastic parameters of the model. Bar parameters (Young's modulus E, yield stress Y_b and plastic modulus H_b) represent the actual sheet material properties and are obtained directly from standard uniaxial tensile tests. Hinge parameters (rotational yield moment Y_h, plastic modulus H_h) are effective parameters that must be calibrated because a crease's stiffness and strength depend on its geometry as well as the base material. The calibration follows a procedure combining experimental characterization and finite-element simulation [19,69]. The detailed calibration procedure is demonstrated in the simple fold example below. The same approach has been applied to all examples in this article.

Algorithm 1 Adaptively Damped Newton-Raphson Method (Displacement Control)

Require:
$k_{\max} > 0,\ N_{\text{tol}} > 0,\ \beta_{\min} > 0,\ c_{\min} > 0,\ \text{tol} > 0,\ h_0 > 0,\ \mathbf{d},\ N_{\max} > 0,\ R_{\max} > 0$

$\mathbf{u}^0 \leftarrow \mathbf{0},\ \beta_0 \leftarrow 1,\ c_0 \leftarrow 1,\ N_0 \leftarrow 0$ ▷ Initial state at step 0
for $i = 1$ to $N_{\max}$ **do**
  $h_i \leftarrow \beta_{i-1} \cdot h_0$ ▷ Step size for current increment
  $\mathbf{u}_0^i \leftarrow \mathbf{u}^{i-1} + h_i \cdot \mathbf{d}$ ▷ Initial displacement of step i
  $k \leftarrow 0,\ \text{err} \leftarrow 1$
  while err $>$ tol **and** $k < k_{\max}$ **do**
    $k \leftarrow k + 1$
    $\mathbf{T}_{k-1}^i \leftarrow \mathbf{T}\left(\mathbf{u}_{k-1}^i\right)$ ▷ Internal force vector
    $\mathbf{K}_{k-1}^i \leftarrow \nabla\mathbf{T}\left(\mathbf{u}_{k-1}^i\right)$ ▷ Tangent stiffness matrix
    Solve $\mathbf{K}_{k-1}^i\, \Delta\mathbf{u}_k^i = -\mathbf{T}_{k-1}^i$ ▷ Newton correction
    $\mathbf{u}_k^i \leftarrow \mathbf{u}_{k-1}^i + c_{i-1} \cdot \Delta\mathbf{u}_k^i$ ▷ Damped update
    $\text{err} \leftarrow \left\|\Delta\mathbf{u}_k^i\right\|$
  end while
  if $k \geq k_{\max}$ **or** err $>$ tol **then**
    $N_{i-1} \leftarrow N_{i-1} + 1$ ▷ Accumulate failure count
    if $N_{i-1} \geq R_{\max}$ **then**
      break ▷ Terminate if exceeding max retries
    else if $N_{i-1} < N_{\text{tol}}$ **then**
      $\beta_{i-1} \leftarrow \max\left(\beta_{i-1}/2,\ \beta_{\min}\right)$ ▷ Shrink step factor
    else
      $\beta_{i-1} \leftarrow \max\left(\beta_{i-1},\ 1.0\right) \cdot 1.5$ ▷ Raise to reference then enlarge
      $c_{i-1} \leftarrow \max\left(0.75 \cdot c_{i-1},\ c_{\min}\right)$ ▷ Reduce damping
    end if
    $i \leftarrow i - 1$ ▷ Retry current increment
  else
    $\mathbf{u}^i \leftarrow \mathbf{u}_k^i$ ▷ Save converged displacement
    $N_i \leftarrow 0$ ▷ Reset failure counter
    $c_i \leftarrow 1$ ▷ Reset damping to reference value 1
    if $\beta_{i-1} < 1$ **then**
      $\beta_i \leftarrow \min\left(1.1 \cdot \beta_{i-1},\ 1.0\right)$ ▷ Recover to reference step
    else
      $\beta_i \leftarrow \max\left(0.9 \cdot \beta_{i-1},\ 1.0\right)$ ▷ Fall back to reference step
    end if
  end if
end for

(a) A simple fold

This example serves as the calibration benchmark for the elasto-plastic hinge model. The structure consists of two isosceles right triangular panels connected by a single crease line AB (figure 4a). The triangular panel ABC is fully fixed, while a prescribed rotation is applied to the free panel ABD to induce folding. The material is aluminium.

To obtain a reference for calibration, a high-fidelity simulation is first performed using Abaqus. The crease line is modelled with a reduced thickness (one-fifth of the panel) to mimic localized flexibility. The material properties in Abaqus are: mass density $2.7 \times 10^{-9}\,\text{kg}\,\text{mm}^{-3}$, Young's modulus $E = 67\,000\,\text{MPa}$, Poisson's ratio $\nu = 0.33$ and plasticity defined by yield stresses 250 and 350 MPa at plastic strains 0 and 0.5, respectively (linear hardening). A displacement-controlled rotation is applied, and the moment–rotation curve $M(\theta)$ of the crease is extracted (figure 4b).

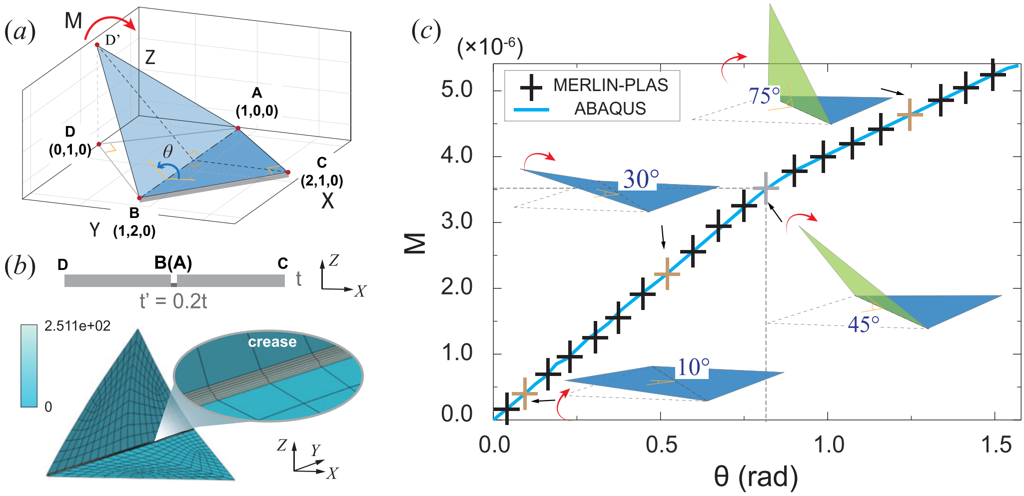

Figure 4. The simple fold example. (a) Geometry and boundary conditions. (b) Abaqus simulation: initial side view and deformed configuration with von Mises stress contour. (c) Moment–rotation response of crease AB: comparison between the Abaqus model and the calibrated MERLIN-PLAS model.

The same fold is then simulated with the proposed elasto-plastic bar-and-hinge model. The bar elements are assigned the same Young's modulus and plastic parameters as the aluminium sheet. The hinge parameters (total yield moment and plastic modulus) are adjusted until the $M(\theta)$ curve matches the Abaqus reference. The calibrated dimensionless values are: folding hinge yield moment $Y_{h,f} = 1.6$, folding hinge plastic modulus $H_{h,f} = 5$, bending hinge yield moment $Y_{h,b} = 5$ and bending hinge plastic modulus $H_{h,b} = 0.5$. The calibrated values are dimensionless in the MERLIN-PLAS input file because the software adopts a consistent unit system where all quantities are entered without explicit units. Figure 4c compares the moment–rotation curves obtained from Abaqus and the bar-and-hinge model. The excellent agreement validates the calibration, demonstrating that the model captures the elasto-plastic behaviour of a single crease with good accuracy. The displacement-controlled simulation completed 500 increments with exactly three iterations per increment, demonstrating robust convergence for this verification case. Unless otherwise stated, the same calibration strategy can be applied to the folding hinges in the subsequent examples.

(b) Eggbox: folding and unloading of a non-Euclidean origami

The Eggbox pattern is a classic example of non-Euclidean origami, as it cannot be folded from a flat sheet without inducing permanent deformation or residual stress [51]. To test whether the proposed elasto-plastic bar-and-hinge model can capture residual-stress-driven shape changes, we simulate the folding of an Eggbox unit from a flat configuration to a fully folded state, followed by complete unloading to zero applied moment.

The Eggbox unit consists of four diamond-shaped panels arranged around a central vertex O. The initial configuration is flat. The boundary conditions and the deformation sequence are illustrated in figure 5a. A displacement-controlled load is applied to node S_4 in the negative y-direction, gradually increasing until S_4 reaches the position of the fully fixed node S_3, at which point the Eggbox becomes fully folded. The load is then reversed until the bending moment in the folding hinges returns to zero. Due to structural symmetry, the moment–rotation responses of hinges OS_1, OS_2 and OS_5 are identical; therefore, we present only the results for hinge OS_2 in the following.

The material parameters are: Young's modulus of bars $E = 10^6$; bar yield stress $Y_b = 10^6$; folding hinge yield moment $Y_{h,f} = 0.1$; folding hinge plastic modulus $H_{h,f} = 0.1$; bending hinge

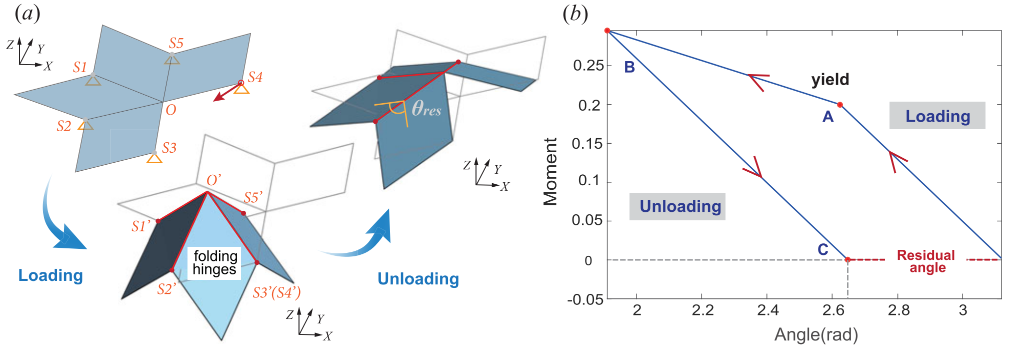

Figure 5. (a) Deformation sequence of the Eggbox unit: left: initial flat configuration with boundary conditions (node O free; S_1, S_2, S_5 constrained in z; S_4 constrained in x and z; S_3 fully fixed); middle: fully folded Eggbox configuration; right: configuration after unloading to zero moment. (b) Moment–rotation response of hinge OS_2.

yield moment $Y_{h,b} = 1$ and bending hinge plastic modulus $H_{h,b} = 1$. The bar cross-sectional area is set to $A = 0.01$, and the folding and bending stiffness coefficients are $k_f = 0.2$ and $k_b = 1$, respectively. The displacement-controlled simulation converged in four iterations per increment without any failure, demonstrating robust solver performance for this non-Euclidean folding and unloading process.

Figure 5b shows the moment–rotation response of hinge OS_2. A clear yield point is observed at $\theta \approx 2.6$ rad, followed by a plastic plateau. Upon unloading, the moment returns to zero, but the rotation angle does not recover to the initial value; a residual rotation angle θ_{res} remains. This residual rotation is a direct consequence of plastic deformation, leading to permanent deformation that prevents full elastic recovery.

This example demonstrates that the proposed elasto-plastic bar-and-hinge model can simulate residual-stress-driven non-Euclidean folding by naturally accumulating plastic strain in the hinges. For applications where detailed panel-wise residual stress is critical, the framework can be extended by introducing an equivalent initial strain field, which we leave for future work.

(c) The Sareh twist in a rectangular sheet

The fourfold polygonal unit recently studied by Kresling [70] exhibits twisting behaviour that distinguish it from simpler patterns. Interestingly, the underlying kinematic principle of this twist is intimately related to the 'Sareh twist' [71–75], of which the asymmetric folding of a rectangle via crease lines passing through its four vertices is a specific case. This fundamental twist unit serves as the geometric primitive for more complex twisting systems, such as the helical tessellation known as 'Sareh non-trivial tessellation' [70]. We therefore simulate this elementary configuration to provide a direct test of the proposed elasto-plastic bar-and-hinge model.

A rectangular sheet $ABCD$ with side lengths $a = 2.0$ and $b = 1.5$ is considered (figure 6a). Following the analytical solution of Sareh [71], the interior node N is placed on the hyperbolic curve that guarantees flat-foldability of the resulting degree-4 vertex. The triangular panel BNC is fully fixed in space. The fold lines are assigned as follows: BN is a mountain fold, while AN, DN and CN are valley folds. An active folding force is applied to panel ABN, causing it to rotate clockwise about hinge BN (active folding). This active rotation induces a passive counter-clockwise rotation of panel DNC about hinge NC (passive folding), generating the characteristic twisting motion (figure 6b,c). The simulation is performed in force-controlled mode.

The material parameters are as follows: folding hinge stiffness coefficient $k_f = 0.2$; bending hinge stiffness coefficient $k_b = 2$; folding hinge yield moment $Y_{h,f} = 0.02$; folding hinge plastic modulus $H_{h,f} = 0.1$; bending hinge yield moment $Y_{h,b} = 0.2$; bending hinge plastic modulus $H_{h,b} = 1$. The bar cross-sectional area is $A = 0.01$.

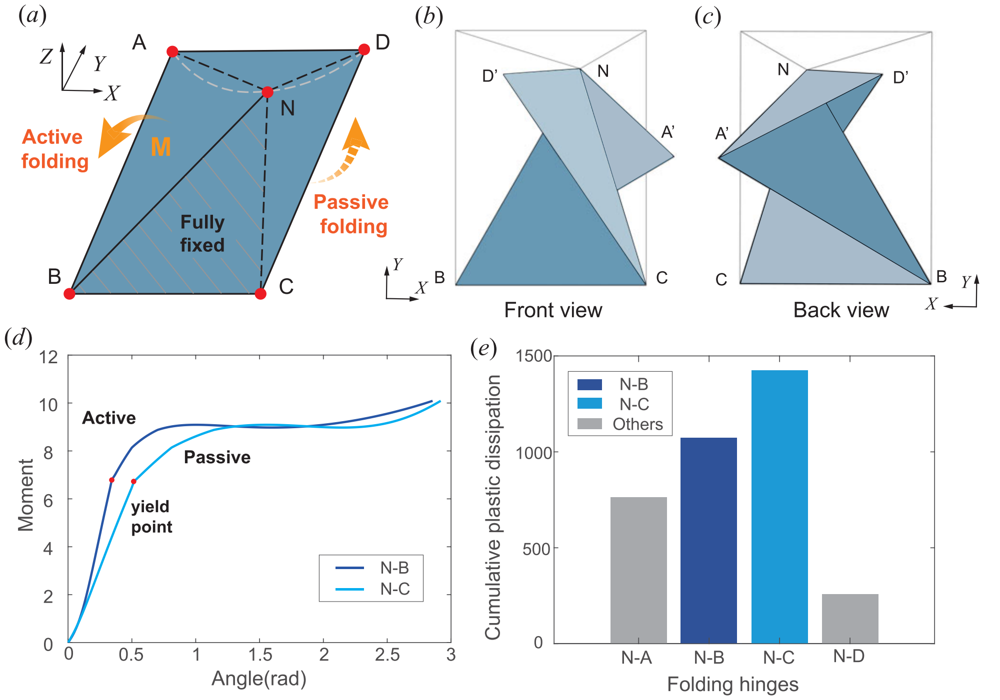

Figure 6. A rectangular Sareh unit. (a) Initial configuration of the rectangular sheet with node *N* lying on the hyperbolic curve (dashed). (b) Front view of the folded state. (c) Back view of the folded state. (d) Moment–rotation responses of the four folding hinges. (e) Plastic energy dissipated by each hinge during the folding process.

The moment–rotation responses of the four folding hinges are plotted in figure 6d. The active hinge *BN* yields first, as indicated by the clear deviation from linearity at a rotation angle of approximately 0.35 rad. Shortly thereafter, the passive hinge *NC* also enters the plastic regime, driven by the kinematic coupling between the two panels. The folding continues until the entire assembly folds into a nearly flat state. The energy dissipated by each hinge during the folding process is shown in figure 6e. Hinges *BN* and *NC* dominate the plastic energy absorption, while the contributions of *AN* and *ND* are negligible. This behaviour is consistent with the physical observation that the twist is primarily accommodated by the two diagonal hinges that connect the moving panels to the fixed triangular base. From the numerical perspective, the solver converged reliably for this force-controlled twisting problem. The iteration count per increment was 3 or 4. No divergence or increment failure occurred, confirming the robustness of the arc-length method for this geometrically nonlinear twisting deformation.

The successful simulation of this fundamental twist unit demonstrates that the proposed elasto-plastic bar-and-hinge model captures the essential features of asymmetric folding: the sequence of plastic yielding in active and passive hinges, the induced twisting kinematics and the distribution of energy dissipation. By validating the model on this geometric primitive, we provide strong evidence for its capability to accurately simulate more complex twisting systems, such as the fourfold polygonal twist, by assembling such basic units.

(d) Morph origami

The Morph origami [19,75,76] is a reconfigurable pattern that transitions seamlessly between the Miura and Eggbox modes. Its non-developable, degree-4 unit cell enables substantial shape changes. By selectively adjusting creases, the surface topography of peaks and valleys can be programmed, allowing direct control over the effective Poisson's ratio. This design also exhibits topological mode locking, which stabilizes the structure throughout its transformation.

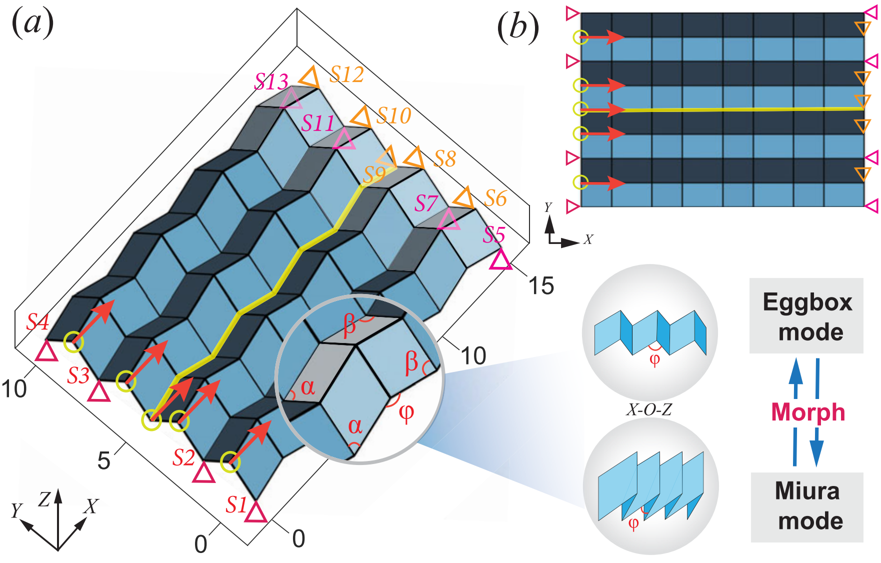

Figure 7. Morph origami. (a) Initial configuration and boundary conditions of Morph structure. The angle ϕ is 112.61°, α is 65.25° and β is 60.00°. Supports S_1–S_4 constrain displacements exclusively in the z-direction; S_6, S_8–S_{10} and S_{12} restrict motion solely in the y-direction; S_5, S_7, S_{11} and S_{13} impose constraints on both y- and z-displacements. Nodes along the yellow line are restricted from moving in the x-direction. The transition between Eggbox and Miura configurations in the Morph system is governed by the ϕ angle. (b) Top view of Morph structure.

The elasto-plastic analysis of the Morph origami during the mode-switching process remains underexplored. This study addresses this gap by investigating a Morph structure subjected to a sequence of compressive and tensile displacement loadings. To accurately capture the mechanical behaviour of the structure, the material parameters are defined as follows: Young's modulus of bars $E = 1 \times 10^4$; bar yield stress $Y_b = 200$; bar plastic modulus $H_b = 1 \times 10^3$; folding hinge stiffness coefficient $k_f = 0.2$; bending hinge stiffness coefficient $k_b = 2$; folding hinge yield moment $Y_{h,f} = 0.02$; bending hinge yield moment $Y_{h,b} = 0.2$; folding hinge plastic modulus $H_{h,f} = 0.1$; bending hinge plastic modulus $H_{h,b} = 1$. These parameters are critical for modelling the elasto-plastic behaviour of the Morph structure under loading conditions. The geometry and boundary conditions are depicted in figure 7. The displacement-controlled simulation converged consistently in four iterations per increment without any failure, confirming the solver's stability during the mode-switching process.

The behaviour of the Morph structure is characterized by analysing the force–displacement curve throughout the entire deformation process, as shown in figure 8. Initially, the load factor is zero. Yielding occurs after a short range of elastic deformation at state (i). When the Morph origami is undergoing mode switching between the Eggbox and Miura modes at states (ii) and (iii), the force decreases. At state (iv), the loading direction is reversed. Until state (v), the force returns to zero.

Furthermore, we can see from figure 8b that at mode-switching state (ii), φ_1 decreases rapidly while $\varphi_2, \varphi_3, \varphi_4$ remain nearly unchanged. Here, φ_i $(i = 1, 2, 3, 4)$ represent the dihedral angles between adjacent layers in the Morph structure, as illustrated in figure 8c. Similarly, at mode-switching state (iii), $\varphi_1, \varphi_3, \varphi_4$ almost remain unchanged, while φ_2 decreases rapidly. The mode switching is an unstable process as the origami undergoes large deformation in the absence of additional external loading. Due to plasticity, the final configuration is more folded compared with the initial configuration.

In conclusion, this study establishes a foundational understanding of how elasto-plastic behaviour governs the mode-switching mechanics of Morph structures. These insights provide

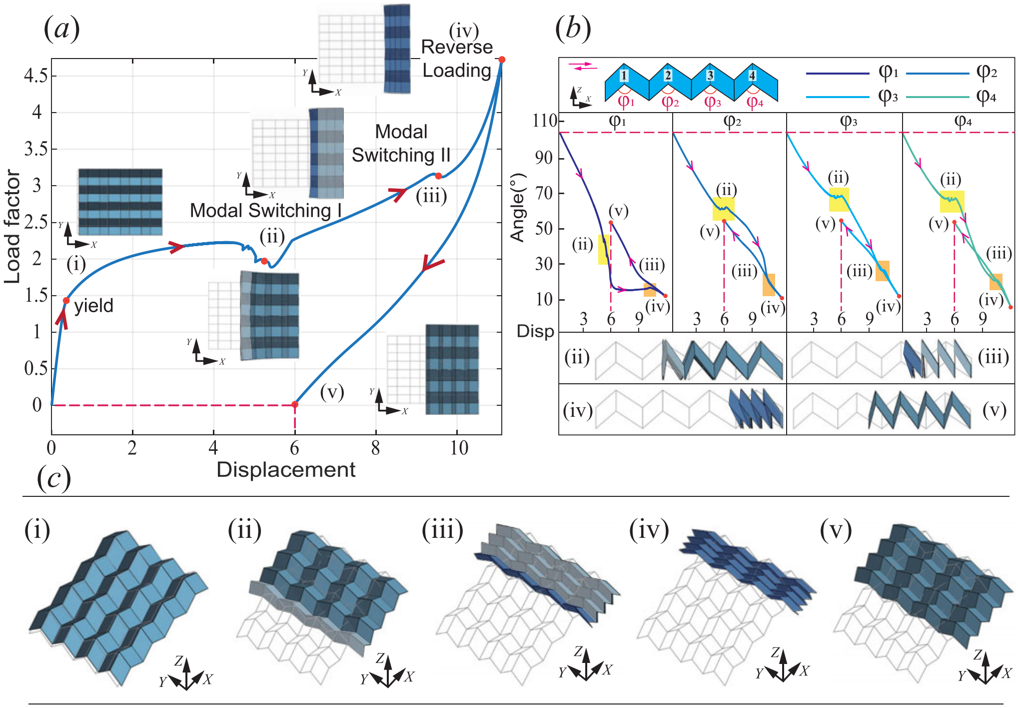

Figure 8. Loading and unloading of Morph origami. (a) Load factor–displacement curve, the mode switching are labelled. (b) Angle φ_i–displacement curve of each layer. (c) The diagram of deformation.

a basis for designing and controlling morphing systems with tailored energy absorption and deformation pathways. For the Morph origami, the mode transition is primarily driven by hinge rotations, with plastic yielding concentrated in folding hinges, while bars experience limited plastic stretching at stress concentrations.

(e) Pop-through defect of the Miura-ori

The Miura-ori pattern is renowned for its high folding ratio and negative Poisson's ratio. Although the Miura-ori is known as a rigid origami, non-rigid deformations could also occur in reality. A notable non-rigid deformation phenomenon of the Miura-ori is known as the 'pop-through defect' [77]. This deformation is bistable, enabling the structure to reversibly snap between two stable configurations, significantly enriching the mechanical functionality of the Miura-ori [78–80].

As shown in figure 9, a vertical force induces the 'pop-through' event, where panel bending leads to a dynamic transition between stable states. This bistable behaviour is both fundamentally interesting and advantageous for designing functional materials and adaptive engineering systems.

The material parameters are defined as follows: Young's modulus of bars $E = 1 \times 10^4$; bar yield stress $Y_b = 30$; bar plastic modulus $H_b = 1 \times 10^3$; folding hinge stiffness coefficient $k_f = 0.2$; bending hinge stiffness coefficient $k_b = 2$; folding hinge yield moment $Y_{h,f} = 0.02$; bending hinge yield moment $Y_{h,b} = 0.2$; folding hinge plastic modulus $H_{h,f} = 0.1$; bending hinge plastic modulus $H_{h,b} = 1$. Here, we discuss the different behaviour under four yield stresses (varying Y_b). The geometry and boundary conditions are depicted in figure 9. It is worth noting that the boundary conditions employed in this work are specifically designed to allow transverse deformation while still triggering the pop-through phenomenon. Comparative tests show that fixing all four edges suppresses snapback, whereas restraining the front and back edges fails to produce a

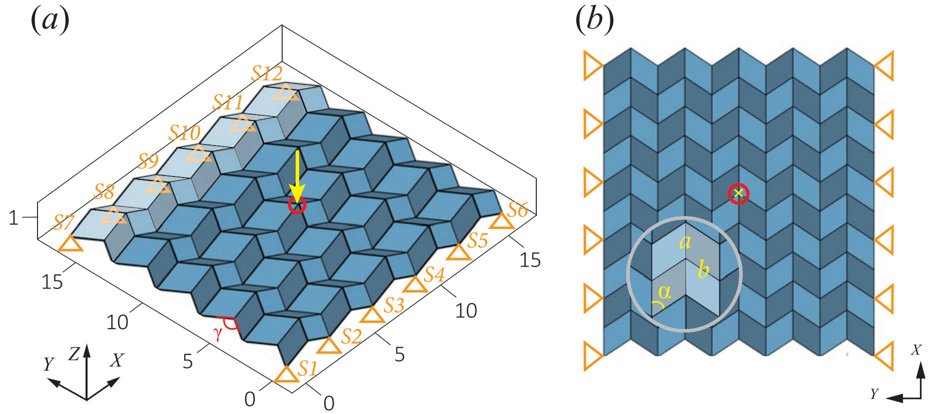

Figure 9. (a) Initial configuration and boundary conditions of the Miura-ori structure. The angle γ is 112.61°. Support S_1 constrains displacements in the *x*-, *y*- and *z*-directions, S_2–S_6 restrict motion in the *y*- and *z*-directions, and S_7 fixes *x*- and *z*-displacements. From S_8 to S_{12}, restrictions only apply in the *z*-direction. A unit load is applied in the −*z*-direction to the node highlighted by a red circle. (b) The top view of a Miura-ori structure, including a flat Miura-ori unit cell. We set $a = 0.02$, $b = 0.02$ and $\alpha = 60°$.

snap-through due to anisotropy. Therefore, the current set-up represents the most appropriate choice for investigating this phenomenon. The force-controlled solver completed 350 increments with an average of 5.3 iterations per step and no failures, demonstrating robust convergence for this snapback problem.

Our analysis delves into the deformation process that leads to the 'pop-through' state within elasto-plastic origami. By understanding the underlying mechanics, we enable new deformation modes for designing materials and structures leveraging the unique properties of the Miura-ori folding pattern.

Figure 10a illustrates the force–displacement response of the Miura-ori under varying yield stresses. The curves exhibit classical bistability, characterized by a snap-through behaviour. Analysis indicates that higher yield stresses suppress plastic deformation, causing the response to converge towards the hyperelastic prediction. This trend confirms that structures with greater yield strength behave in a more predominantly elastic manner.

Furthermore, a distinct snapback phenomenon is observed in the elasto-plastic model with $Y_b = 30$ at a displacement of approximately 3 units. In this process, the central panel's downward motion drives the adjacent elements, culminating in a stable equilibrium configuration where the internal forces balance the applied load, preventing further deformation. The attainment of such stable states is crucial for the safety and performance of structures under load. These results underscore the critical influence of yield stress on the resulting mechanical behaviour and stability. Notably, for $Y_b = 40$, the load–displacement curve begins to develop a concave shape, indicating an incipient tendency towards snapback, although the actual snapback does not yet occur. This gradual transition confirms that the snapback phenomenon does not appear abruptly but diminishes continuously with increasing yield stress. To further investigate the influence of post-yield hardening on the snapback behaviour, we performed additional simulations with fixed yield stress $Y_b = 30$ and varying plastic moduli $H_b = 500$, 1000, 1500 and 2000. The results reveal a clear positive correlation: at $H_b = 500$, snapback does not occur, although an incipient tendency is observed; at $H_b = 1000$, snapback occurs; and at $H_b = 2000$, the snapback becomes most pronounced. This indicates that a higher plastic modulus, which leads to stronger hardening after yielding, facilitates snapback instability, whereas a lower plastic modulus suppresses it (figure 10b).

Although the deformed configurations for $Y_b = 30$ and $Y_b = 70$ appear similar (figure 11), the former undergoes extensive plastic yielding while the latter remains nearly elastic—a distinction

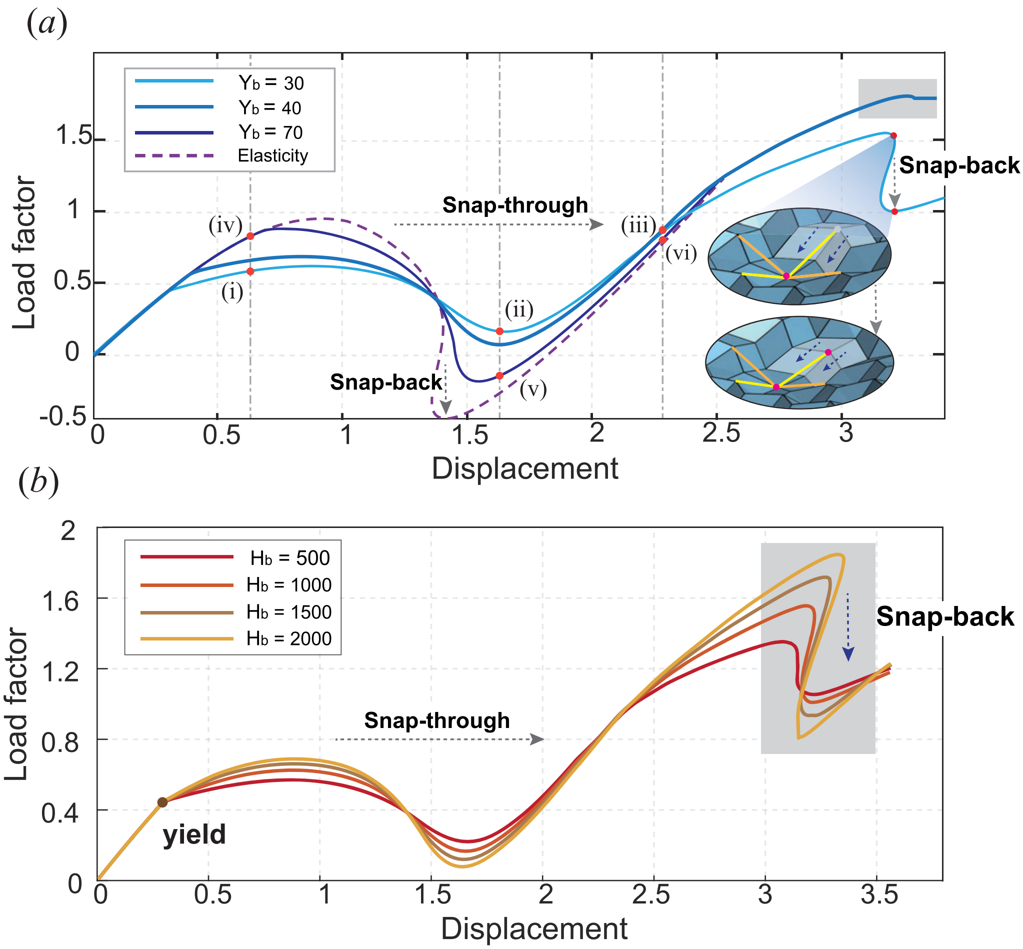

Figure 10. (a) Equilibrium path during the deformation process of a 'pop-through defect' on Miura-ori for the four cases of $Y_b = 30, 40, 70$ and elasticity, respectively. The insets show zoom-in views of the snapback deformation of the centre and its adjacent cells at $Y_b = 30$. (b) Snapback behaviour for different plastic moduli $H_b = 500, 1000, 1500, 2000$ at fixed $Y_b = 30$.

evident in the force–displacement curves rather than in the instantaneous shapes. In the Miura-ori snapback simulation with $Y_b = 30$, plastic yielding is not confined to the bending hinges; bars in the central region also undergo plastic deformation due to the large membrane stretching induced by the pop-through defect. This demonstrates that bar plasticity, while typically secondary to hinge plasticity in thin-sheet origami, can become active in regions of high local stretching. The pop-through defect involves local panel bending, represented as plastic rotation in bending hinges. Hinge plasticity dominates this process.

(f) Cyclic loading of Kresling: hysteresis loop

The Kresling pattern, a sophisticated cylindrical origami configuration, is renowned for its multi-stable behaviour. Its geometry is defined by nodes positioned at the intersections of two longitudinal helices and a transverse circle, creating a mechanically stable and structurally intricate unit cell. This unique arrangement facilitates multiple stable states, enhancing its versatility for engineering applications [81,82].

Experimental studies on paper-based Kresling prototypes confirm the occurrence of elasto-plastic deformation under mechanical load [83–85]. This inelastic behaviour plays a critical role in the structure's actuation performance and influences the transmission of mechanical waves.

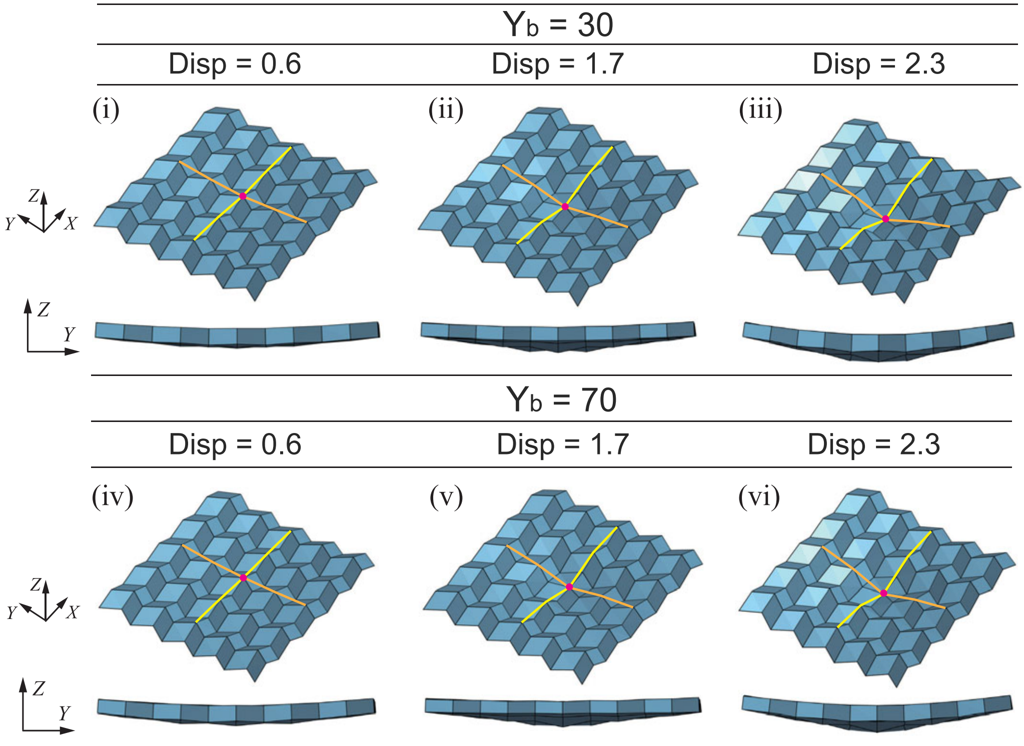

Figure 11. Several key frames of deformed configurations during simulation at $Y_b = 30$ and $Y_b = 70$, corresponding to six points on the equilibrium path ((i)–(iii), (iv)–(vi)).

Under cyclic loading, the force–displacement response deviates from a simple reversible path, forming instead a pronounced hysteresis loop that signifies energy dissipation. This hysteresis stems from differences in energy absorption and release during loading and unloading, resulting in a characteristic phase lag between force and displacement.

The geometry and initial configuration of the Kresling are defined by the side length of top and bottom hexagons, initial height and initial rotational angle; here, we assign the side length $a = 1$, height $h_0 = 1$ and angle $\theta_0 = 11\pi/18$. The material parameters are defined as follows: Young's modulus of bars $E = 1 \times 10^4$; bar yield stress $Y_b = 200$; bar plastic modulus $H_b = 1 \times 10^3$; folding hinge stiffness coefficient $k_f = 0.2$; bending hinge stiffness coefficient $k_b = 2$; folding hinge yield moment $Y_{h,f} = 0.02$; bending hinge yield moment $Y_{h,b} = 0.2$; folding hinge plastic modulus $H_{h,f} = 0.1$; bending hinge plastic modulus $H_{h,b} = 1$. The displacement-controlled simulation converged in exactly three iterations per increment with no failures, demonstrating robust performance for the cyclic loading problem.

Based on the experimental work of Hiromi Yasuda *et al.* [59], who conducted 200 loading–unloading cycles on a Kresling origami unit to obtain hysteresis loops, we performed corresponding simulations using MERLIN-PLAS. Our simulations systematically varied the plastic modulus parameters to further investigate this cyclic behaviour. The results demonstrate that a lower plastic modulus leads to slower convergence of the force–displacement curves, indicating more pronounced plastic deformation accumulation during the initial cycles.

Figure 12b reveals several key phenomena observed during cyclic loading. First, the emergence of hysteresis loops in the force–displacement response indicates significant energy dissipation, primarily due to internal friction and plastic deformation. Second, the gradual reduction in hysteresis loop area with successive cycles reflects material hardening and diminishing energy dissipation. Third, accumulated plastic deformation causes a progressive shift in the force–displacement response, demonstrating the ratcheting effect of permanent structural changes.

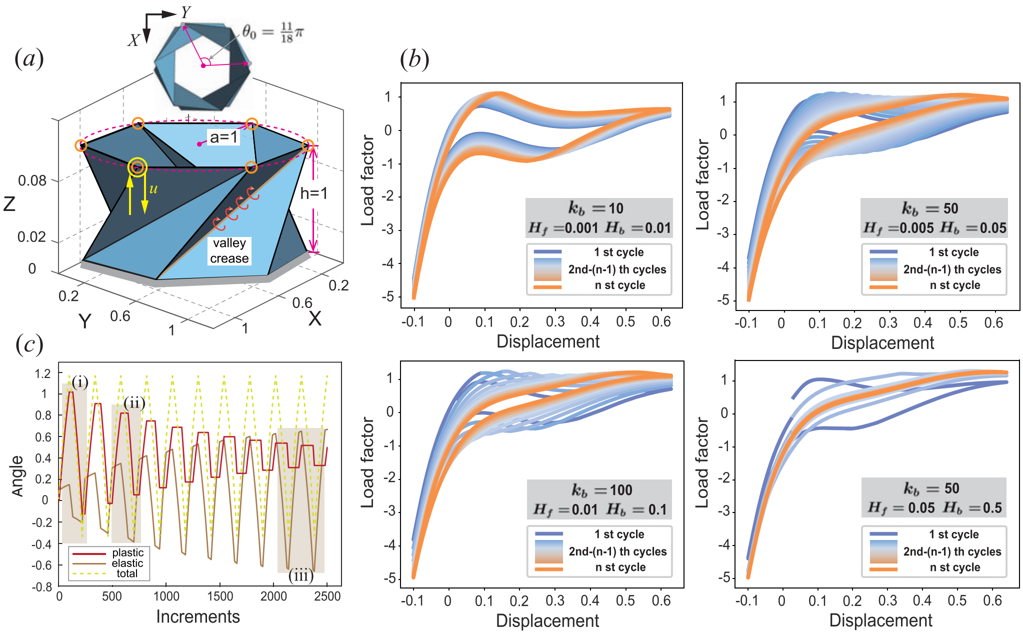

Figure 12. Cyclic loading of Kresling. (a) Initial configuration and boundary conditions of Kresling origami. The height of the structure is $h = 1$, the base profile is a regular hexagonal shape that lies within a circle of radius $r = 1$, and in top view, $\theta_0 = \frac{11}{18}\pi$. Solid grey lines indicate support points, all of which limit displacement in the x-, y- and z-directions. Cyclic displacement loads are applied in the z-direction of the orange-circled nodes. Displacement is measured as the z-displacement of the node labelled with a yellow circle. (b) Force–displacement curves for n cycles of loading/unloading under four different material parameters. The colour gradient indicates the number of cycles. (c) Trends of the elastic and plastic angular components in the valley creases marked in (a) with iteration during cyclic loading.

Finally, after sufficient cycles, the response stabilizes with minimal inter-cycle variation, indicating consistent mechanical behaviour.

These observations are reproduced by MERLIN-PLAS simulations, which particularly highlight the role of plastic modulus in convergence behaviour. Lower plastic moduli—associated with higher plasticity—lead to slower convergence, as the structure undergoes more extensive plastic deformation before reaching stabilization. These findings provide crucial insights into the cyclic mechanics of Kresling origami, with direct implications for energy dissipation applications and structural design.

Figure 12c illustrates the evolution of angular deformation components during cyclic loading. In stage (i), elastic deformation dominates the response. Stage (ii) shows nearly equal contributions from both elastic and plastic components, while in stage (iii), plastic deformation clearly dominates. This progression indicates the emergence of the ‘plastic shakedown’ phenomenon [86–89]: initial loading cycles induce localized yielding at crease regions, accumulating plastic deformation. With continued cycling, the internal stress distribution reaches a stable state where structural transitions can be accomplished through elastic deformation alone, ultimately achieving plastic shakedown. Under cyclic loading, hinge plasticity accumulates rapidly and dominates hysteresis behaviour, whereas bar plasticity develops gradually under axial forces and saturates earlier. Hinges thus constitute the primary source of energy dissipation. While the current rate-independent model does not include fatigue damage accumulation, the extracted plastic strain amplitudes from stabilized hysteresis loops could be used in future work to estimate low-cycle fatigue life via empirical strain–life relations.

5. Conclusion

This research presents MERLIN-PLAS, an elasto-plastic formulation for the structural analysis of origami structures modelled using arbitrary bar-and-hinge configurations. Building upon existing hyperelastic bar-and-hinge frameworks, the proposed formulation incorporates rate-independent elasto-plasticity with isotropic hardening to capture irreversible deformation processes such as energy dissipation and permanent folding. The model decomposes total strain into elastic and plastic components for both bars and rotational hinges and employs a return mapping algorithm to enforce consistency with yield conditions at each incremental step. The formulation enables stable and accurate simulation of origami structures undergoing large displacements and deformations. Adopting small elastic strains within the additive plasticity framework simplifies the constitutive updates, thereby enhancing computational efficiency.

Numerical simulations on several representative origami systems—encompassing simple folds, morphing structures, bistable Miura-ori and the Kresling pattern—demonstrate that the proposed model successfully captures key elasto-plastic phenomena. These include plastic yielding under cyclic loading, hysteresis in force–displacement response and the accumulation of permanent deformation during mode transitions. The model reproduces experimental behaviours such as snap-through instabilities and cyclic energy dissipation, validating its applicability across a wide range of origami-inspired systems.

The proposed elasto-plastic bar-and-hinge model assumes that plastic deformation concentrates at hinges and bars. Consequently, it does not capture distributed plastic yielding within the panels themselves. This limitation is inherent to the reduced-order nature of the bar-and-hinge framework, which is designed primarily to capture global deformation patterns, load–displacement responses, and energy dissipation characteristics. For problems where detailed panel plasticity is essential, a continuum-based shell finite-element model remains the recommended approach. Additionally, the current model employs a linear isotropic hardening law for both bars and hinges. While this provides a clear and computationally efficient description of plastic behaviour, it may not accurately represent the cyclic softening, progressive stiffening or stiffness degradation observed in some real origami creases. For such materials, more advanced constitutive models including nonlinear kinematic or isotropic hardening or damage-coupled plasticity would be required. The current framework can accommodate these extensions by simply replacing the hardening rule, which we intend to pursue in future work. Thus, the model is well suited for design exploration and parametric studies where rapid assessment of global elasto-plastic behaviour is needed, while recognizing the aforementioned limitations.

Compared with purely hyperelastic models, the elasto-plastic formulation offers a more realistic representation of origami structures that exhibit irreversible deformations and energy loss under cyclic loads. This capability is especially relevant for practical applications where durability and reliability are essential, such as deployable aerospace systems, biomedical devices and reconfigurable robotics.

The flexibility of the formulation invites further extensions, including the incorporation of strain rate effects, anisotropic hardening and multi-layered or composite origami assemblies. Future work may also address dynamic loading conditions and global contact interactions. The proposed model provides a versatile and efficient computational framework that enhances the realism and predictive power of origami structural analysis, paving the way for broader adoption in engineering applications.

Ethics. This work did not involve any active collection of human or animal data, as it is entirely based on computational simulations. No ethical approval was required.

Data accessibility. This article has no additional data.

Declaration of AI use. We have not used AI-assisted technologies in creating this article.

Authors' contributions. Y.T.: data curation, investigation, methodology, validation, writing—original draft, writing—review and editing; Y.C.: investigation, writing—review and editing; Y.M.: investigation, writing—review and editing; Y.Z.: investigation, writing—review and editing; K.L.: conceptualization, formal analysis,

funding acquisition, investigation, methodology, project administration, resources, software, supervision, validation, visualization, writing—review and editing.

All authors gave final approval for publication and agreed to be held accountable for the work performed therein.

Conflict of interest declaration. We declare we have no competing interests.

Funding. K.L. and Y.T. were supported by the National Natural Science Foundation of China through grant 12372159, and Beijing Natural Science Foundation through grant no. L254067.

Disclaimer. The information provided in this paper is the sole opinion of the authors and does not necessarily reflect the views of the sponsoring agencies.

Acknowledgements. The authors acknowledge the High-Performance Computing Platform at Peking University for providing computational resources. We are grateful to Prof. Tongxi Yu for his insightful discussions and guidance on origami mechanics. We thank Prof. Glaucio H. Paulino for suggesting the name 'MERLIN-PLAS' for the code.

References

1. Lin Z, Novelino LS, Wei H, Alderete NA, Paulino GH, Espinosa HD, Krishnaswamy S. 2020 Folding at the microscale: enabling multifunctional 3D origami-architected metamaterials. *Small* **16**, 2002229. (doi:10.1002/smll.202002229)
2. Zhai Z, Wu L, Jiang H. 2021 Mechanical metamaterials based on origami and kirigami. *Appl. Phys. Rev.* **8**, 041319. (doi:10.1063/5.0051088)
3. Bertoldi K, Vitelli V, Christensen J, Van Hecke M. 2017 Flexible mechanical metamaterials. *Nat. Rev. Mater.* **2**, 1–11. (doi:10.1038/natrevmats.2017.66)
4. Chen T, Bilal OR, Lang R, Daraio C, Shea K. 2019 Autonomous deployment of a solar panel using elastic origami and distributed shape-memory-polymer actuators. *Phys. Rev. Appl.* **11**, 064069. (doi:10.1103/PhysRevApplied.11.064069)
5. Pehrson NA, Ames DC, Smith SP, Magleby SP, Arya M. 2020 Self-deployable, self-stiffening, and retractable origami-based arrays for spacecraft. *AIAA J.* **58**, 3221–3228. (doi:10.2514/1.J058778)
6. Morgan J, Magleby SP, Howell LL. 2016 An approach to designing origami-adapted aerospace mechanisms. *J. Mech. Des.* **138**, 052301. (doi:10.1115/1.4032973)
7. Kuribayashi K, Tsuchiya K, You Z, Tomus D, Umemoto M, Ito T, Sasaki M. 2006 Self-deployable origami stent grafts as a biomedical application of Ni-rich TiNi shape memory alloy foil. *Mater. Sci. Eng.: A* **419**, 131–137. (doi:10.1016/j.msea.2005.12.016)
8. Ze Q, Wu S, Dai J, Leanza S, Ikeda G, Yang PC, Iaccarino G, Zhao RR. 2022 Spinning-enabled wireless amphibious origami millirobot. *Nat. Commun.* **13**, 3118. (doi:10.1038/s41467-022-30802-w)
9. Rogers J, Huang Y, Schmidt OG, Gracias DH. 2016 Origami mems and nems. *MRS Bull.* **41**, 123–129. (doi:10.1557/mrs.2016.2)
10. Yan Z *et al.* 2016 Controlled mechanical buckling for origami-inspired construction of 3D microstructures in advanced materials. *Adv. Funct. Mater.* **26**, 2629–2639. (doi:10.1002/adfm.201504901)
11. Rus D, Tolley MT. 2018 Design, fabrication and control of origami robots. *Nat. Rev. Mater.* **3**, 101–112. (doi:10.1038/s41578-018-0009-8)
12. Kim SJ, Lee DY, Jung GP, Cho KJ. 2018 An origami-inspired, self-locking robotic arm that can be folded flat. *Sci. Robot.* **3**, eaar2915. (doi:10.1126/scirobotics.aar2915)
13. Novelino LS, Ze Q, Wu S, Paulino GH, Zhao R. 2020 Untethered control of functional origami microrobots with distributed actuation. *Proc. Natl Acad. Sci. USA* **117**, 24 096–24 101. (doi:10.1073/pnas.2013292117)
14. Chen W, Yang S, Zhu C, Cheng Y, Shi Y, Yu C, Liu K. 2025 Scalable jet swimmer driven by pulsatile artificial muscles and soft chamber buckling. *Adv. Mater.* **37**, 2503777. (doi:10.1002/adma.202503777)
15. Gu J, Li H, Zhang C, Shen Y, Jia S, Tian S, Bai K, Meng X, Xue Z. 2026 Film-assisted shape-locking assembly for complex freestanding 3D electronic architectures. *Adv. Funct. Mater.* **36**, e74736. (doi:10.1002/adfm.74736)
16. Zhu Y, Dong Y, Ji D, Meng X, Xue Z, Fan X, Li Y. 2024 Flexible double-layer adjustable frequency selective surfaces based on 3D cross-shaped kirigami structure. *Adv. Mater. Technol.* **9**, 2301715. (doi:10.1002/admt.202301715)

17. Xue Z *et al.* 2022 Assembly of complex 3D structures and electronics on curved surfaces. *Sci. Adv.* **8**, eabm6922. (doi:10.1126/sciadv.abm6922)
18. Ji Z *et al.* 2022 Morphable three-dimensional electronic mesofliers capable of on-demand unfolding. *Sci. China Mater.* **65**, 2309–2318. (doi:10.1007/s40843-022-2007-8)
19. Misseroni D, Pratapa PP, Liu K, Paulino GH. 2022 Experimental realization of tunable Poisson's ratio in deployable origami metamaterials. *Extr. Mech. Lett.* **53**, 101685. (doi:10.1016/j.eml.2022.101685)
20. Filipov ET, Tachi T, Paulino GH. 2015 Origami tubes assembled into stiff, yet reconfigurable structures and metamaterials. *Proc. Natl Acad. Sci. USA* **112**, 12 321–12 326. (doi:10.1073/pnas.1509465112)
21. Cai J, Ren Z, Ding Y, Deng X, Xu Y, Feng J. 2017 Deployment simulation of foldable origami membrane structures. *Aerosp. Sci. Technol.* **67**, 343–353. (doi:10.1016/j.ast.2017.04.002)
22. Jianguo C, Xiaowei D, Yuting Z, Jian F, Ya Z. 2016 Folding behavior of a foldable prismatic mast with Kresling origami pattern. *J. Mech. Robot.* **8**, 031004. (doi:10.1115/1.4032098)
23. Fang H, Chu SCA, Xia Y, Wang KW. 2018 Programmable self-locking origami mechanical metamaterials. *Adv. Mater.* **30**, 1706311. (doi:10.1002/adma.201706311)
24. Ma J, You Z. 2014 Energy absorption of thin-walled square tubes with a prefolded origami pattern—part I: geometry and numerical simulation. *J. Appl. Mech.* **81**, 011003. (doi:10.1115/1.4024405)
25. Ma J, Song J, Chen Y. 2018 An origami-inspired structure with graded stiffness. *Int. J. Mech. Sci.* **136**, 134–142. (doi:10.1016/j.ijmecsci.2017.12.026)
26. Gattas J, You Z. 2014 Quasi-static impact of indented foldcores. *Int. J. Impact Eng.* **73**, 15–29. (doi:10.1016/j.ijimpeng.2014.06.001)
27. Gattas J.M., You Z.. 2015 The behaviour of curved-crease foldcores under low-velocity impact loads. *Int. J. Solids Struct.* **53**, 80–91. (doi:10.1016/j.ijsolstr.2014.10.019)
28. Lv C, Krishnaraju D, Konjevod G, Yu H, Jiang H. 2014 Origami based mechanical metamaterials. *Sci. Rep.* **4**, 5979. (doi:10.1038/srep05979)
29. Filipov ET, Paulino GH, Tachi T. 2016 Origami tubes with reconfigurable polygonal cross-sections. *Proc. R. Soc. A* **472**, 20150607. (doi:10.1098/rspa.2015.0607)
30. Hauptmann R, Schweizerhof K. 1998 A systematic development of 'solid-shell' element formulations for linear and non-linear analyses employing only displacement degrees of freedom. *Int. J. Numer. Methods Eng.* **42**, 49–69. (doi:10.1002/(SICI)1097-0207(19980515)42:1<49::AID-NME349>3.0.CO;2-2)
31. Ramm E., Wall W.A.. 2004 Shell structures—a sensitive interrelation between physics and numerics. *Int. J. Numer. Methods Eng.* **60**, 381–427. (doi:10.1002/nme.967)
32. Lee PS, Noh HC, Bathe KJ. 2007 Insight into 3-node triangular shell finite elements: the effects of element isotropy and mesh patterns. *Comput. Struct.* **85**, 404–418. (doi:10.1016/j.compstruc.2006.10.006)
33. Otter M, Elmqvist H, Mattsson SE. 2003 The new modelica multibody library. In *3rd International Modelica Conference, Turin, Italy*, pp. 311–330. New York, NY: ASME.
34. Steinbrecher I, Humer A, Vu-Quoc L. 2017 On the numerical modeling of sliding beams: a comparison of different approaches. *J. Sound Vib.* **408**, 270–290. (doi:10.1016/j.jsv.2017.07.010)
35. Castagnetti D, Dragoni E. 2006 Efficient stress analysis of adhesively bonded joints by finite element techniques. In *Engineering systems design and analysis*, vol. 42509, pp. 817–825. Linköping, Sweden: Linköping University Electronic Press.
36. Tachi T. 2010 Geometric considerations for the design of rigid origami structures. In *Proceedings of the International Association for Shell and Spatial Structures (IASS) Symposium*, vol. 12, pp. 458–460. Shanghai, China: Elsevier.
37. Tachi T. 2009 Generalization of rigid-foldable quadrilateral-mesh origami. *J. Int. Assoc. Shell Spat. Struct.* **50**, 173–179.
38. Tachi T. 2009b Simulation of rigid origami. *Origami* **4**, 175–187.
39. Li R, Choi G. 2025 Rigidity control of general origami structures. (http://arxiv.org/abs/2507.16934).
40. Meloni M, Zhang Q, Cai J. 2025 A computational framework for simulating accurate deployment motion paths of rigid foldable origami tessellations. *Comput. Aided Des.*, **140**, 103975.
41. Schenk M, Guest SD. 2011 Origami folding: a structural engineering approach. *Origami* **5**, 291–304.

42. Beaufort NM, Aragon AM. 2024 Miura-ori pattern optimization for origami shape matching using the bar-and-hinge model. Master's Thesis, Delft University of Technology, the Netherlands.
43. Lahiri A, Pratapa PP. 2024 Improving mass lumping and stiffness parameters of bar and hinge model for accurate modal dynamics of origami structures. *Philos. Trans. A* **382**, 20240012.
44. Xu H, Tobasco I, Plucinsky P. 2024 Derivation of an effective plate theory for parallelogram origami from bar and hinge elasticity. *J. Mech. Phys. Solids* **192**, 105832. (doi:10.1016/j.jmps.2024.105832)
45. Sironi T, Cinefra M, Troise A. 2024 Multilayer and multifield analysis of origami deployable structures. *Mater. Res. Proc.* **42**, 162–168.
46. Liu K, Novelino LS, Gardoni P, Paulino GH. 2020 Big influence of small random imperfections in origami-based metamaterials. *Proc. R. Soc. A* **476**, 20200236.
47. Liu K, Paulino GH. 2017 Nonlinear mechanics of non-rigid origami: an efficient computational approach. *Proc. R. Soc. A* **473**, 20170348. (doi:10.1098/rspa.2017.0348)
48. Liu K, Paulino G. 2018 Highly efficient nonlinear structural analysis of origami assemblages using the MERLIN2 software. *Origami* **7**, 1167–1182.
49. Grey S, Scarpa F, Schenk M. 2018 Local actuation of tubular origami. In *The 7th International Meeting on Origami in Science, Mathematics and Education (7OSME), Oxford, UK*. The 7OSME Organizing Committee.
50. Cehula J. 2019 Deformations of light activated shape memory polymers. Master's Thesis, Charles University, Czech Republic.
51. Liu KT, Paulino G. 2024 Geometric mechanics of hybrid origami assemblies combining developable and non-developable patterns. *Proc. R. Soc. A* **480**, 20230716. (doi:10.1098/rspa.2023.0716)
52. Wu S, Zhao T, Zhu Y, Paulino GH. 2024 Modular multi-degree-of-freedom soft origami robots with reprogrammable electrothermal actuation. *Proc. Natl Acad. Sci. USA* **121**, e2322625121. (doi:10.1073/pnas.2322625121)
53. Zhu Y, Birla M, Oldham KR, Filipov ET. 2020 Elastically and plastically foldable electrothermal micro-origami for controllable and rapid shape morphing. *Adv. Funct. Mater.* **30**, 2003741. (doi:10.1002/adfm.202003741)
54. van Manen T, Janbaz S, Ganjian M, Zadpoor AA. 2020 Kirigami-enabled self-folding origami. *Mater. Today* **32**, 59–67. (doi:10.1016/j.mattod.2019.08.001)
55. Zhang G, Zhao Q, Yang L, Zou W, Xi X, Xie T. 2016 Exploring dynamic equilibrium of Diels–Alder reaction for solid state plasticity in remoldable shape memory polymer network. *ACS Macro Lett.* **5**, 805–808. (doi:10.1021/acsmacrolett.6b00357)
56. Zhao Q, Zou W, Luo Y, Xie T. 2016 Shape memory polymer network with thermally distinct elasticity and plasticity. *Sci. Adv.* **2**, e1501297. (doi:10.1126/sciadv.1501297)
57. Khazaaleh S, Dalaq AS, Daqaq MF. 2024 An origami-inspired energy absorber. *Smart Mater. Struct.* **33**, 045029. (doi:10.1088/1361-665X/ad3361)
58. Tan B, Liu K. 2024 Quantized energy absorption of sandwiched origami ring. *Extr. Mech. Lett.* **70**, 102183. (doi:10.1016/j.eml.2024.102183)
59. Yasuda H, Miyazawa Y, Charalampidis EG, Chong C, Kevrekidis PG, Yang J. 2019 Origami-based impact mitigation via rarefaction solitary wave creation. *Sci. Adv.* **5**, eaau2835. (doi:10.1126/sciadv.aau2835)
60. Zhou Y, Li X, Zhang Y, Feng J, Cai J. 2024 Hysteresis analysis on origami energy dissipation braces with local Miura units. *Acta Mech. Solida Sin.* **37**, 700–710. (doi:10.1007/s10338-024-00503-6)
61. Nickabadi S, Askari Sayar M, Alirezaeipour S, Ansari R. 2025 Origami-inspired auxetic structures: design and performance in quasi-static and dynamic loading. *Mech. Based Des. Struct. Mach.* **53**, 4435–4464. (doi:10.1080/15397734.2025.2450519)
62. Zhang J, Chen J, Wang C. 2025 Study on energy dissipation in origami-inspired composite structures. In *Structures*, vol. 79, p. 109571. Amsterdam, the Netherlands: Elsevier.
63. Wriggers P. 2008 *Nonlinear finite element methods*. Berlin, Germany: Springer Science & Business Media.
64. Bonet J, Wood RD. 1997 *Nonlinear continuum mechanics for finite element analysis*. Cambridge, UK: Cambridge University Press.
65. Horák M, Jirásek M. 2013 An extension of small-strain models to the large-strain range based on an additive decomposition of a logarithmic strain. In *Programs and algorithms of numerical*

*mathematics*s (eds J Chleboun, K Segeth, J Šístek, T Vejchodský), pp. 88–93. Prague, Czech Republic: Institute of Mathematics AS CR.

66. Xiao H, Bruhns OT, Meyers A. 2000 A consistent finite elastoplasticity theory combining additive and multiplicative decomposition of the stretching and the deformation gradient. *Int. J. Plast.* **16**, 143–177. (doi:10.1016/S0749-6419(99)00045-5)
67. Li L. 2024 Geometric nonlinear analysis based on the generalized displacement control method and orthogonal iteration. *Nonlinear Eng.* **13**, 20240047. (doi:10.1515/nleng-2024-0047)
68. Yang Y, Pang B, Xu H, Liu L, Chen A. 2025 Embedded secant predictor for tracing the multi critical postbuckling response based on generalized displacement control method. *Eng. Struct.* **345**, 121457. (doi:10.1016/j.engstruct.2025.121457)
69. Filipov E, Liu K, Tachi T, Schenk M, Paulino GH. 2017 Bar and hinge models for scalable analysis of origami. *Int. J. Solids Struct.* **124**, 26–45. (doi:10.1016/j.ijsolstr.2017.05.028)
70. Kresling B. 2026 The Sareh twist: a hidden geometric principle in origami tessellations. *J. Appl. Phys.* **139**, 084904. (doi:10.1063/5.0304558)
71. Sareh P. 2019 The least symmetric crystallographic derivative of the developable double corrugation surface: computational design using underlying conic and cubic curves. *Mater. Des.* **183**, 108128. (doi:10.1016/j.matdes.2019.108128)
72. Sareh P, Guest SD. 2015 A framework for the symmetric generalisation of the Miura-ori. *Int. J. Space Struct.* **30**, 141–152. (doi:10.1260/0266-3511.30.2.141)
73. Lu C, Chen Y, Shi J, Gao J, Lv H, Shen Z, Sareh P. 2025 Inverse design of tubular energy absorbers formed from the least-symmetric crystallographic DDC surface. *Int. J. Solids Struct.* **320**, 113508. (doi:10.1016/j.ijsolstr.2025.113508)
74. Sareh P. 2014 Symmetric descendants of the Miura-ori. PhD Dissertation, University of Cambridge, UK.
75. Pratapa PP, Liu K, Paulino GH. 2019 Geometric mechanics of origami patterns exhibiting Poisson's ratio switch by breaking mountain and valley assignment. *Phys. Rev. Lett.* **122**, 155501. (doi:10.1103/PhysRevLett.122.155501)
76. Liu K, Tachi T, Paulino GH. 2021 Bio-inspired origami metamaterials with metastable phases through mechanical phase transitions. *J. Appl. Mech.* **88**, 091002. (doi:10.1115/1.4050556)
77. Silverberg JL, Evans AA, McLeod L, Hayward RC, Hull T, Santangelo CD, Cohen I. 2014 Using origami design principles to fold reprogrammable mechanical metamaterials. *Science* **345**, 647–650. (doi:10.1126/science.1252876)
78. Khosravani MR, Anders D, Ayatollahi MR, Reinicke T. 2025 Fabrication of mechanical metamaterials by 3D printing: recent advancements and current challenges. *Arch. Civ. Mech. Eng.* **25**, 244. (doi:10.1007/s43452-025-01290-8)
79. Song K, Li H, Li Y, Ma J, Zhou X. 2024 A review of curved crease origami: design, analysis, and applications. *Front. Phys.* **12**, 1393435. (doi:10.3389/fphy.2024.1393435)
80. Yan P, Huang H, Meloni M, Li B, Cai J. 2025 Mechanical properties inside origami-inspired structures: an overview. *Appl. Mech. Rev.* **77**, 011001. (doi:10.1115/1.4066566)
81. Masana R, Dalaq AS, Khazaaleh S, Daqaq MF. 2024 The Kresling origami spring: a review and assessment. *Smart Mater. Struct.* **33**, 043002. (doi:10.1088/1361-665X/ad2f6f)
82. Zhang J, Wang C. 2024 Deployment behavior and mechanical property analysis of Kresling origami structure. *Compos. Struct.* **341**, 118234. (doi:10.1016/j.compstruct.2024.118234)
83. Kong L, Zhao YF. 2025 From origami to bistable and laminate structures: a review for multifunctional applications from structural perspective of shape-changing structures. *Adv. Intell. Syst.* **8**, 2500505. (doi:10.1002/aisy.202500505)
84. Alipour SM, Arghavani J. 2024 Elastic energy trapping in Kresling origami. *Mech. Adv. Mater. Struct.* **31**, 11 755–11 770. (doi:10.1080/15376494.2024.2311844)
85. Zhang J, Liu S, Gao T, Wang C. 2025 Kresling origami structure: mechanical and aerodynamic drag characteristics. *Compos. Struct.* **357**, 118962. (doi:10.1016/j.compstruct.2025.118962)
86. Sawczuk A. 1974 Shakedown analysis of elastic-plastic structures. *Nucl. Eng. Des.* **28**, 121–136. (doi:10.1016/0029-5493(74)90091-0)
87. Hung ND, Morelle P. 1990 Plastic shakedown analysis. In *Mathematical programming methods in structural plasticity* (ed. DL Smith), pp. 181–205. Berlin, Germany: Springer.
88. Reinhardt W. 2008 A noncyclic method for plastic shakedown analysis. . *J. Pressure Vessel Technol.* **130**, 031209. (doi:10.1115/1.2937760)
89. Rad MM. 2018 A review of elasto-plastic shakedown analysis with limited plastic deformations and displacements. *Period. Polytech., Civ. Eng.* **62**, 812–817.